A&A 518, A59 (2010)
DOI: 10.1051/0004-6361/200913430

Astronomy & Astrophysics

Observations and modeling of the dust emission from the H_2-bright galaxy-wide shock in Stephan's Quintet

P. Guillard[1,2], F. Boulanger[1], M. E. Cluver[2], P. N. Appleton[3], G. Pineau des Forêts[1,4], and P. Ogle[2]

[1] Institut d'Astrophysique Spatiale (IAS), UMR 8617, CNRS, Université Paris-Sud 11, Bâtiment 121, 91405 Orsay Cedex, France
e-mail: pierre.guillard@ias.u-psud.fr
[2] *Spitzer* Science Center, IPAC, California Institute of Technology, Mail code 100-22, Pasadena, CA 91125, USA
[3] NASA *Herschel* Science Center (NHSC), IPAC, California Institute of Technology, Mail code 100-22, Pasadena, CA 91125, USA
[4] LERMA, UMR 8112, CNRS, Observatoire de Paris, 61 avenue de l'Observatoire, 75014 Paris, France

Received 8 October 2009 / Accepted 28 March 2010

ABSTRACT

Context. *Spitzer Space Telescope* observations have detected powerful mid-infrared (mid-IR) H_2 rotational line emission from the X-ray emitting large-scale shock ($\sim 15 \times 35$ kpc^2) associated with a galaxy collision in Stephan's Quintet (SQ). Because H_2 forms on dust grains, the presence of H_2 is physically linked to the survival of dust, and we expect some dust emission to originate in the molecular gas.

Aims. To test this interpretation, IR observations and dust modeling are used to identify and characterize the thermal dust emission from the shocked molecular gas.

Methods. The spatial distribution of the IR emission allows us to isolate the faint PAH and dust continuum emission associated with the molecular gas in the SQ shock. We model the spectral energy distribution (SED) of this emission, and fit it to *Spitzer* observations. The radiation field is determined with *GALEX* UV, *HST* *V*-band, and ground-based near-IR observations. We consider two limiting cases for the structure of the H_2 gas: it is either diffuse and penetrated by UV radiation, or fragmented into clouds that are optically thick to UV.

Results. Faint PAH and dust continuum emission are detected in the SQ shock, outside star-forming regions. The 12/24 μm flux ratio in the shock is remarkably close to that of the diffuse Galactic interstellar medium, leading to a Galactic PAH/VSG abundance ratio. However, the properties of the shock inferred from the PAH emission spectrum differ from those of the Galaxy, which may be indicative of an enhanced fraction of large and neutrals PAHs. In both models (diffuse or clumpy H_2 gas), the IR SED is consistent with the expected emission from dust associated with the warm (>150 K) H_2 gas, heated by a UV radiation field of intensity comparable to that of the solar neighborhood. This is in agreement with *GALEX UV* observations that show that the intensity of the radiation field in the shock is $G_{\rm UV} = 1.4 \pm 0.2$ [Habing units].

Conclusions. The presence of PAHs and dust grains in the high-speed ($\sim$1000 km s^{-1}) galaxy collision suggests that dust survives. We propose that the dust that survived destruction was in pre-shock gas at densites higher than a few 0.1 cm^{-3}, which was not shocked at velocities larger than $\sim$200 km s^{-1}. Our model assumes a Galactic dust-to-gas mass ratio and size distribution, and current data do not allow us to identify any significant deviations of the abundances and size distribution of dust grains from those of the Galaxy. Our model calculations show that far-IR *Herschel* observations will help in constraining the structure of the molecular gas, and the dust size distribution, and thereby to look for signatures of dust processing in the SQ shock.

Key words. atomic processes – ISM: general – dust, extinction – galaxies: clusters: individual: Stephan's Quintet – shock waves – infrared: ISM

1. Introduction

Stephan's Quintet (Hickson Compact Group HCG92, Arp 319, hereafter SQ) is an extensively studied compact group of four interacting galaxies that have a complex dynamical history (e.g., Allen & Sullivan 1980; Moles et al. 1997). A remarkable feature of SQ is that a giant ($\approx 15 \times 35$ kpc) shock is created by an intruding galaxy, NGC 7318b (Sbc pec), colliding into NGC 7319's tidal tail, at a relative velocity of $\sim$1000 km s^{-1}. Evidence of a group-wide shock comes from observations of an extended X-ray ridge containing shock-heated ($\sim 5 \times 10^6$ K) gas (Pietsch et al. 1997; Trinchieri et al. 2003, 2005; O'Sullivan et al. 2009), strong radio synchrotron emission from the radio-emitting plasma (Allen & Hartsuiker 1972; Sulentic et al. 2001; Williams et al. 2002; Xu et al. 2003), and shocked-gas excitation diagnostics from optical emission lines (Xu et al. 2003). This extended region is denoted *"ridge"* or simply *"SQ shock"* in this paper.

Observations with the infrared spectrograph (*IRS*, Houck et al. 2004) onboard the *Spitzer Space Telescope* have revealed a powerful mid-infrared (mid-IR) H_2 rotational line emission from warm ($\sim 10^2$–10^3 K) molecular gas in the SQ shock (Appleton et al. 2006; Cluver et al. 2010). The H_2 emission is extended not only over the whole ridge, but in several other structures, including an extension towards the Seyfert galaxy NGC 7319, and the intergalactic starburst SQ-A (Xu et al. 1999). The latter structure, beyond the northern tip of the ridge, has been shown to contain significant CO-emitting gas (Gao & Xu 2000; Smith & Struck 2001; Lisenfeld et al. 2002). To explain the H_2 emission from the SQ ridge, Guillard et al. (2009) considered the collision of two flows of multiphase dusty gas and proposed a model that quantifies the gas cooling, dust destruction, H_2 formation and excitation in the postshock medium. In their scenario, the H_2 gas

is formed from gas that is shocked to velocities sufficiently low (V_s < 200 km s^{-1}) for dust to survive. Because H_2 molecules form on dust grains (e.g., Cazaux & Tielens 2004), dust is a key element in this scenario.

Xu et al. (1999, 2003) reported detection of diffuse far-infrared (hereafter FIR) emission from the intergalatic medium (hereafter IGM) with the *Infrared Space Observatory (ISO)*, and proposed that the dust emission in the shock region would arise from dust grains that efficiently cool the X-ray emitting plasma via collisions with hot electrons. The FIR emission would then trace the structure of the shock, as suggested by Popescu et al. (2000) for the case of shocks driven into dusty gas that is accreting onto clusters of galaxies. However, the poor spatial resolution of these observations makes it difficult to separate the dust emission associated with star formation (in the neighborhood galaxies, or SQ-A) from that really associated with the shock. In addition, Guillard et al. (2009) show that the dust contribution to the cooling of the hot ($\sim 5 \times 10^6$ K) plasma is expected to be low, because of efficient thermal sputtering of the grains. If we assume that the age of the galaxy collision is $\sim 5 \times 10^6$ yrs, grains smaller than 0.1 μm in radius must have been destroyed. However, the plasma could still be dusty if, before the shock, a significant fraction of the dust mass was in larger grains and/or if dust destruction is balanced by mass exchange between the cold and the hot gas phases (Guillard et al. 2009).

The discovery of bright H_2 emission in the ridge triggered new perspectives about the origin of the dust emission in the SQ ridge. In the context of our model for the H_2 formation in the SQ shock, we expect some dust emission from the molecular gas. We use *Spitzer* observations and a model of the dust emission to test this expectation. *Spitzer* observations show that the bright polycyclic aromatic hydrocarbons (henceforth PAHs) and mid-IR continuum emitting regions are spatially correlated with UV emission and associated with star-forming regions mainly related to the individual sources in the group (in particular the spiral arm of the intruder galaxy NGC 7318b) and with SQ-A (Cluver et al. 2010; Natale et al., in prep.). These IR-bright regions do not correlate with the radio, X-ray, or H_2 line emission, which trace the shock structure. In this paper, we focus on the fainter dust emission from the SQ ridge itself, outside these star-forming regions. The spatial distribution of the mid-IR emission allows us to isolate the dust emission from the shock. The UV, visible, and near-IR observations determine the spectral energy distribution (hereafter SED) of the radiation field used as an input to the dust model. We consider two limiting cases for the structure of the molecular gas, either diffuse, or fragmented into clouds that are optically thick to UV light. An updated version of the Désert et al. (1990) model is used to compute the dust emission from molecular gas in these two cases, and fit the model results to the observed IR SED in the SQ shock. The Galactic dust size distribution is taken as a reference.

This paper is organized as follows. Section 2 presents the new IR *Spitzer* observations of SQ, and the UV, optical, and near-IR ancillary data we used in this paper. The method used to perform photometry within the SQ shock region and the results are described in Sect. 3. Section 4 presents the *Spitzer* imaging and spectroscopy results pertaining to the dust emission in the shock structure, emphasizing the PAH properties in the shock. The physical framework and inputs of the dust modeling are outlined in Sect. 5, and the results are discussed and compared to the mid-IR *Spitzer* observations in Sect. 6. In Sect. 7, we discuss the dust processing in the shock. We then present our conclusions in Sect. 8 and propose new observations to constrain the physical structure of the molecular gas in the shock.

In this paper we assume the distance to the SQ group to be 94 Mpc (with a Hubble constant of 70 km s^{-1} Mpc^{-2}) and a systemic velocity for the group as a whole of 6600 km s^{-1}. At this distance, 10 arcsec = 4.56 kpc.

2. Observations of the Stephan's Quintet shock

In the following paragraphs, we present the new mid-IR (Sect. 2.1) observations of SQ, and the ancillary UV (Sect. 2.2.1), optical (Sect. 2.2.2), and near-IR (Sect. 2.2.3) data, respectively.

2.1. Spitzer IR imaging and spectroscopy

Stephan's Quintet has been imaged with the *InfraRed Array Camera* (*IRAC*, Fazio et al. 2004) at 3.6, 4.5, 5.8, 8 μm, with the *IRS* blue peak-up imager (PUI) at 16 μm, and with the *Multiband Imaging Photometer for Spitzer* (*MIPS*, Rieke et al. 2004) at 24 and 70 μm. The 70 μm image was reported in Xu et al. (2008). The pixel sizes are 1.8″, 2.45″, and 5″ at 16, 24, and 70 μm, respectively. Except for the 70 μm image, we direct the reader to Cluver et al. (2010) for a description of the observational details and data reduction. The upper right panel of Fig. 1 shows the 16 μm data from the *IRS* blue *PUI*. The bottom left and right panels show the *MIPS* 24 and 70 μm images.

The SQ shock region was also mapped with the *IRS* spectrograph (Cluver et al. 2010). The Short-Low (SL) and Long-Low (LL) modules of the spectrograph were used, covering the wavelength ranges 5.3−14.0 and 14−38 μm, with spectral resolution of $\lambda/\delta\lambda$ = 60−127 and 57−126, respectively.

2.2. Ancillary data

We present the UV, optical, and near-IR ancillary data we used to determine the radiation field heating the dust (Sect. 5.2).

2.2.1. *GALEX* UV imaging

The upper left corner of Fig. 1 shows the near-UV (NUV) image from the *Galaxy Evolution Explorer* mission (*GALEX,* Martin et al. 2005). These observations were reported by Xu et al. (2005). The pixel size is 1.5″, the wavelength is λ = 2267 Å, and the bandwith is $\Delta\lambda$ = 732 Å. The far-UV (FUV) image (λ = 1516 Å, $\Delta\lambda$ = 268 Å) was also used but is not shown here.

If one were to exclude the foreground galaxy NGC 7320 (Sd), most of the UV emission would be associated with the two spiral members of the group, NGC 7319 and NGC 7318b, and the intragroup medium starburst SQ-A. The galaxy-wide shock structure, which shows up in Hα, radio, and X-ray observations, is barely visible in the UV images. Based on the comparison between *ISO* and *GALEX* data, Xu et al. (2005) concluded that most of the UV emission in the ridge is not associated with the large-scale shock itself, but with H II regions along the spiral arm of the intruder NGC 7318b.

We use the flux calibration described in both the *GALEX* observer's guide[1] and Morrissey et al. (2007). The unit data number (DN, or 1 count per second, cps) is equivalent to 108 and 36 μJy for FUV and NUV, or, equivalently, 1.4×10^{-15} and 2.06×10^{-16} erg s^{-1} cm^{-2} Å^{-1}, respectively. We do not apply any aperture correction to the extended source UV photometry on

[1] http://galexgi.gsfc.nasa.gov/docs/galex/

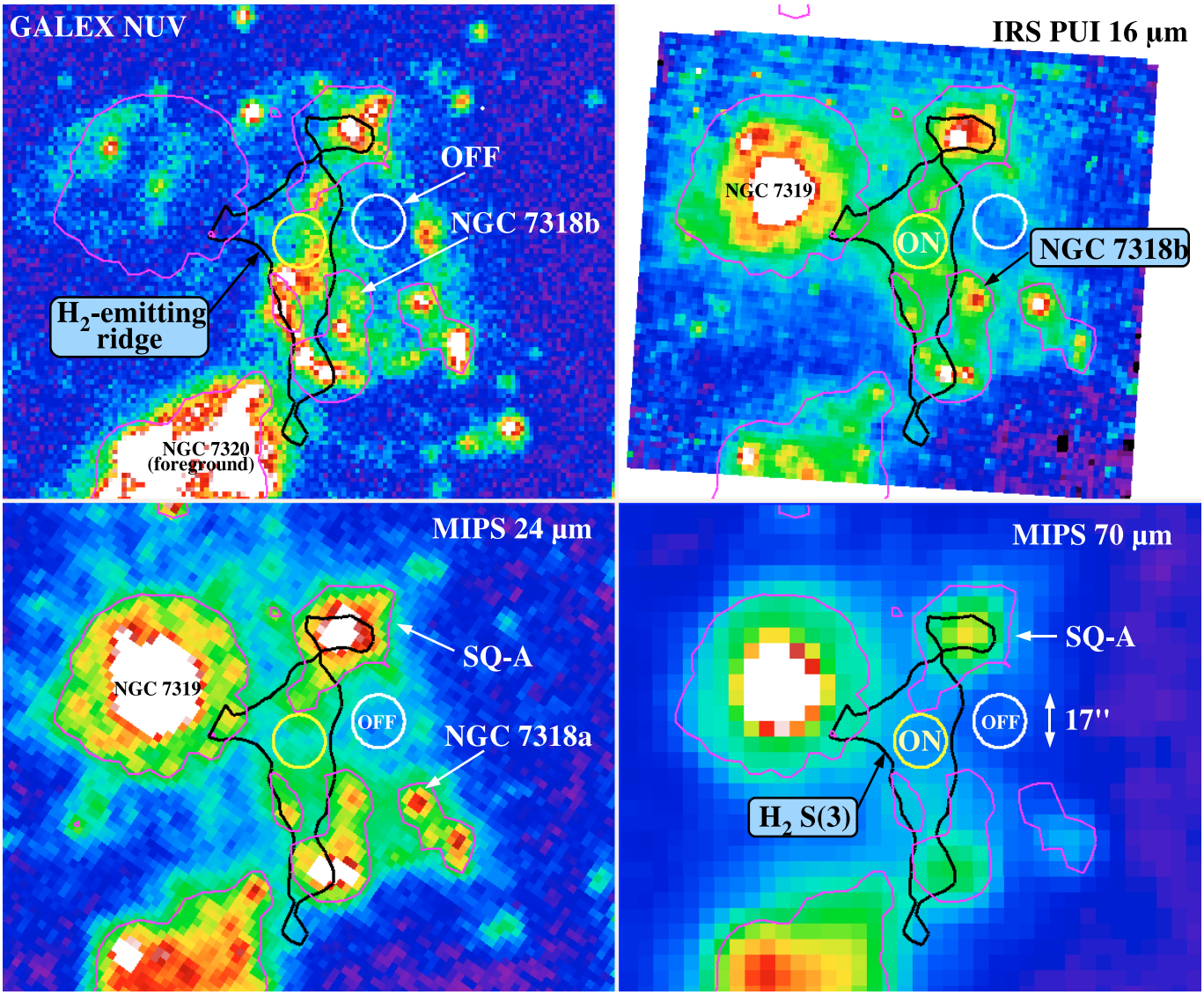

Fig. 1. UV and mid-IR observations of Stephan's Quintet. *Top-left* is a near-UV (2 267 Å) *GALEX* image from Xu et al. (2005), *top-right* is the *Spitzer IRS* 16 μm peak-up image, *bottom-left* and *bottom-right* are the 24 μm and 70 μm *Spitzer MIPS* images of the SQ group, respectively. For all images, the black contours shows the 4σ (0.3 MJy sr^{-1}) 0–0 S(3) H_2 line emission detected over the SQ ridge, from *Spitzer IRS* mapping by Cluver et al. (2010). The magenta contours show the 24 μm emission at a 0.25 MJy sr^{-1} level. They were used to identify star-forming regions that overlap the H_2 contours in the ridge. Photometry was performed within the H_2 contours, excluding or not excluding these star-forming regions. The circles indicate 17″ beams where aperture photometry was also performed. The yellow circle shows the "ON" position in the SQ shock, centered on α = 22h35′59.8″, δ = +33°58′16.7″. The white circle show the "OFF" position we used to subtract the background signal, centered on α = 22h35′57.7″, δ = +33°58′23″.

GALEX images since the PSF full width half maxima (*FWHM*) are 4.9″ and 4.2″ for the NUV and FUV, respectively.

2.2.2. HST *V*-band imaging with WFPC2

We used *V*-band data taken with the *Wide Field Planetary Camera 2 (WFPC2)* onboard the *Hubble Space Telescope (HST)*. For the *F569W* filter, the data consist of two sets of two images (4 × 800 s exposure in total), each set for a given dithering position. The data were first processed by the *HST* pipeline. After alignment of the images with the IRAF data reduction software, a median combination of the four images was taken, followed by the removal of the remaining hot pixels by a 3 × 3 pixels median filter. We obtained a *V*-band image similar to that presented in Gallagher et al. (2001).

The photometry were performed using the flux calibration given in the header of the images (1 DN = 4.149 × 10^{-21} W m^{-2} Å^{-1}). The central wavelength of the *F569W* *V*-band filter is λ = 5 644.4 Å.

2.2.3. Near-IR *WIRC* imaging

We used near-IR (NIR) data from deep observations with the Wide field IR Camera (*WIRC*) on the Palomar 200-inch telescope (V. Charmandaris, private communication). The *WIRC* images were taken in July, 2009 and processed with the *Swarp* software[2]. They are 5 mag deeper than the corresponding *2MASS* images. The zero-point magnitudes are 24.50, 22.73, and 23.05, so we used flux calibrations of 0.252, 0.830, and 0.402 μJy DN^{-1}

[2] http://astromatic.iap.fr/software/swarp

for J, H, and K_s, respectively. The corresponding central wavelengths used are 1.235 ± 0.006, 1.662 ± 0.009, and 2.159 ± 0.011 μm. The images show that most of the NIR emission in the SQ ridge is associated with the spiral arm of the intruder, NGC 7318b. NIR emission associated with the SQ-A northern starburst is also detected.

3. Photometry on IR, optical, and UV images

We describe the method used to perform the photometry on *Spitzer* mid-IR images for the dust emission and on near-IR, optical, and UV images to estimate the radiation field at the position of the SQ shock.

3.1. Method

3.1.1. Dust emission

The SQ field of view is a crowded region (see Sect. 4.1 for a description of the spatial distribution of the dust emission). To isolate the dust emission from the shock itself, we summed the signal within regions that are not contaminated by IR-emitting, star-forming regions. Since the shock is surrounded by bright sources, we did not apply any aperture correction. For comparison, three different area were used to perform photometric measurements.

1. The signal was summed over a circular aperture of 17″ in diameter that is centered on the SQ ridge, in the middle of the X-ray emitting shock front. This 17″ aperture corresponds to the *FWHM* of the MIPS beam at $\lambda = 70$ μm. It is marked with the yellow circle in Fig. 1 ("ON" position).
2. The signal was integrated over the SQ ridge within the H_2 contours (black line in Fig. 1) that define the shock structure. Except SQ-A, star-forming regions within the black H_2 emission contour were included. They are defined by the 24 μm iso-flux ($F_{24\,\mu m} > 0.25$ MJy sr^{-1}) contour (magenta line in Fig. 1).
3. The signal was summed over the SQ ridge within the H_2 contour but excluding the star forming regions. To do this, we subtract from the signal the emission arising from the intersection of the areas within the magenta 24 μm contours and black H_2 contours.

To remove the contamination from the halo of the group, we chose to estimate the background level in a region close to the H_2-emitting shock. This "OFF" region is marked with the white circle in Fig. 1. For the 70 μm image, we cannot exclude that the flux within the "ON" position is contaminated by the brighter sources around it. Thus, we consider our 70 μm flux as an upper limit. A more detailed analysis of the *MIPS* 70 and 160 μm images will be reported in Natale et al. (in prep.).

3.1.2. Radiation field

The radiation field is the integral of the flux over all directions. In the UV domain, due to scattering of light, we can assume that the radiation field is isotropic and estimate its strength from UV photometry at the position of the shock. Thus, we measured the UV fluxes within the same apertures as for the *Spitzer* images, using the same "OFF" position.

The UV fluxes were corrected for both foreground galactic and SQ internal extinctions. For the extinction curve of the Galactic diffuse interstellar medium ($R_V = 3.1$ curve in Weingartner & Draine 2001a), the visible extinction $A_V^{(MW)} = 0.24$ scales to the FUV and NUV Galactic extinctions at *GALEX* wavelengths, respectively $A_{FUV}^{(MW)} = 0.62$ and $A_{NUV}^{(MW)} = 0.72$. We used the Xu et al. (2005) values for the internal SQ extinction, i.e., $A_{FUV}^{(SQ)} = 0.76$ and $A_{NUV}^{(SQ)} = 0.88$.

The optical and near-IR images show that the shock is surrounded by bright sources, in particular NGC 7318b and nearby star-forming regions. Since there is little scattering at these wavelengths, the photometry restricted to the shock area is likely to underestimate the optical and near IR intensity of the radiation field. The choice of the aperture is rather arbitrary in that case and only provides a rough approximation of the optical and near-IR radiation field. We note that the photometry was performed after removal of Galactic stars (using the DAOPHOT package).

Based on an average optical extinction of $A_V = 0.6$ (Guillard et al. 2009) for the center position in the ridge, and a Galactic extinction curve, we applied the extinction corrections $A_J = 0.17$, $A_H = 0.11$, and $A_{K_s} = 0.07$ for J, H, and K_s bands, respectively. We used the values of zero-point fluxes from Cohen et al. (2003), i.e. 1594 ± 28, 1024 ± 20, 666.7 ± 12.6 Jy for J, H, and K_s bands, respectively. The internal extinction correction applied to the *HST* photometry is $A_{F569W} = 0.575$.

3.2. Results

The quantitative results about the photometry performed on IR *Spitzer* images are gathered in Table 1. The surface brightnesses are given for the three areas described above. We estimate from the *IRS* spectrum that the 17 μm S(1) and 8 μm S(4) H_2 line emission represent respectively 68% and 62% of the *IRS* Peak-Up Imager 16 μm and the *IRAC* 8 μm in-band flux within the 17″ ON aperture centered on the shock, and we correct for this contamination. The last row of Table 1 indicates the fluxes we adopt throughout this paper. The error bars are estimated by using two different background subtractions close to the "OFF" position (8-arcsec shifts in the East-West direction). In addition, we include calibration uncertainties (of the order of 5%).

The results of the UV *GALEX* photometry are gathered in Table 2. The surface brightnesses are given for the three apertures defined in Sect. 3.1.1. The UV fluxes measured over the SQ ridge aperture that includes the 24 μm-bright (>0.25 MJy sr^{-1}) regions are 10–25% higher than the fluxes measured when these regions had been removed from the aperture ("SQ ridge (partial)" row). The brightnesses are background-subtracted and corrected for foreground galactic extinction and SQ internal extinction. From the UV surface brightness values, we derive the intensity of the standard interstellar radiation field in Habing units.

The results show that the UV flux in the shock, outside star-forming regions, corresponds to an interstellar radiation field of average intensity $G_{UV} = 1.4 \pm 0.2$ in Habing units[3] (see Sect. 5.2.1 for details). The value of G_{UV} is used to characterize the intensity of the non-ionizing radiation field in the shock (Sect. 5.2). The error bar on the G_{UV} factor takes into account two background subtractions obtained by shifting the OFF position by 8″ in the east-west direction. This uncertainty does not take into account the uncertainty in the optical extinction. Although optical spectroscopy shows that there are spatial variations in the A_V value in the shock ($A_V = 0.1 - 2.5$), we do not expect this to have an important impact on our estimate of G_{UV}, because it is calculated over a large aperture. If the most

[3] The flux of the Habing field ($G_{UV} = 1$) equals 2.3×10^{-3} erg s^{-1} cm^{-2} at $\lambda = 1530$ Å (Habing 1968; Mathis et al. 1983).

Table 1. Summary of the mid-IR photometric measurements[1] performed on the *Spitzer IRAC*, *IRS PUI* 16 μm, and *MIPS* 24, and 70 μm images (Fig. 1).

Target region	3.6 μm	4.5 μm	5.8 μm	8 μm[5]	16 μm[6]	24 μm	70 μm
SQ ridge[2]	23.7 ± 0.9	11.9 ± 0.2	7.3 ± 0.2	4.2 ± 0.1	1.25 ± 0.05	2.25 ± 0.12	<6.43
SQ ridge (partial)[3]	19.4 ± 1.7	9.9 ± 1.8	6.0 ± 0.1	3.35 ± 0.11	1.00 ± 0.06	0.89 ± 0.15	<5.04
17″ beam[4]	17.6 ± 0.9	9.15 ± 0.12	5.29 ± 0.15	3.07 ± 0.11	0.88 ± 0.03	0.79 ± 0.15	<3.91

Notes. The background-subtracted surface brightnesses are indicated for three different apertures. The last row (17″ circular aperture) shows the values we adopt throughout this paper, and in particular for the SED presented in Fig. 2.
(1) Fluxes are in units of $\times 10^{-8}$ W m^{-2} sr^{-1}.
(2) Mid-IR signal integrated over the shock structure, defined by the 4σ S(3) H_2 rotational line contours (black line in Fig. 1). We exclude the SQ-A star-forming region.
(3) Mid-IR signal integrated over the S(3) H_2 rotational line contours by excluding overlaps with the ($\mathcal{F}_{24\ \mu m} > 0.25$ MJy sr^{-1}) 24 μm magenta contours (see Fig. 1). This allows us to partially remove the contribution from star-forming regions to the dust emission.
(4) Mid-IR signal integrated over the 17″ beam in the center of the SQ shock structure (yellow circle in Fig. 1).
(5) The contribution of the 8 μm S(4) H_2 line emission to the 8 μm in-band flux is subtracted.
(6) The contribution of the 17 μm S(1) H_2 line emission to the 16 μm in-band flux is subtracted.

Table 2. Summary of the UV photometric measurements performed on *GALEX* FUV and NUV images (see Fig. 1).

Target position	FUV (λ = 1516 Å)		NUV (λ = 2267 Å)	
	Flux $\times 10^{-7}$ [W m^{-2} sr^{-1}]	Radiation field G [Habing units]	Flux $\times 10^{-7}$ [W m^{-2} sr^{-1}]	Radiation field G [Habing units]
SQ ridge[1]	2.82 ± 0.34	1.54 ± 0.19	2.74 ± 0.39	1.98 ± 0.29
SQ ridge (partial)[2]	2.29 ± 0.35	1.25 ± 0.19	2.25 ± 0.37	1.63 ± 0.29
17″ ON beam[3]	2.49 ± 0.35	1.36 ± 0.19	2.42 ± 0.39	1.75 ± 0.29

Notes. The flux columns indicate surface brightnesses that are corrected for the sky background.
(1) UV signal integrated over the shock structure, defined by the 4σ S(3) H_2 rotational line contours (black line in Fig. 1). We exclude the SQ-A star-forming region.
(2) UV signal integrated over the S(3) H_2 rotational line contours by excluding overlaps with the ($\mathcal{F}_{24\ \mu m} > 0.25$ MJy sr^{-1}) 24 μm magenta contours (see Fig. 1). This allows us to partially remove the contribution from star-forming regions to the dust emission.
(3) UV signal integrated over the 17″ beam at the center of the SQ ridge (yellow circle in Fig. 1).

Table 3. Optical *HST V*-band and near-infrared *WIRC* surface brightnesses[1] in the J, H, and K_s bands for the SQ ridge.

Band	V	J	H	K_s	J:H:K_s
Flux	7.2 ± 1.6	8.45 ± 0.64	8.54 ± 0.65	8.07 ± 0.61	1.048:1.058:1
Dered	12.2 ± 2.9	9.93 ± 0.77	9.44 ± 0.77	8.60 ± 0.75	1.154:1.096:1

Notes. (1) The fluxes are given in units of 10^{-7} W m^{-2} sr^{-1}. "Dered" indicates the extinction-corrected brightness, and the "J:H:K_s" column shows flux ratios between the bands.

extincted regions were to have a reasonably small surface filling factor, they would not affect G_{UV} significantly.

The extinction-corrected surface brightnesses measured on *HST V*-band and *Palomar WIRC* images are gathered in Table 3.

4. Dust emission from Stephan's Quintet: observational results

This section reports the observational results about the dust emission detected in the SQ ridge. We compare the mid-IR SED and the relative intensities of the PAH bands in the SQ shock to that of the Galactic diffuse interstellar medium (ISM).

4.1. Spatial distribution of the dust emission from the SQ group

The images in Fig. 1 show that the bright mid-IR emitting regions are associated with the NGC 7319 galaxy and with UV-luminous, star-forming regions (Cluver et al. 2010). The mid-IR emission does not correlate with the H_2, X-ray, and radio emissions. Interestingly, these star-forming regions are outside the galactic disks of NGC 7318a and b, suggesting that a significant amount of gas has been displaced from these galaxies by tidal interactions. If we exclude the foreground galaxy NGC 7320, the bright mid-IR emission is found to originate in the NGC 7319 galaxy, the SQ-A starburst region, and an arc-like feature to the east of the intruding galaxy NGC 7318b. This arc structure is clearly seen in the UV, IRAC, and 16 μm images, and could be associated with NGC 7318b's spiral arm. The 24 and 70 μm images show a bright and extended emission at the southern tip of the ridge, which may be associated with enhanced star formation in this arc feature.

Dust is detected in the SQ shock region, at a distance of 10−20 kpc of the nearest surrounding galaxies. In the following, we focus on this faint emission observed within the SQ ridge, outside star-forming regions. We note that in the 16 μm *IRS Blue Peak-Up* image, the emission in the ridge correlates well with the H_2 emission, which is caused by the contamination of the H_2 17 μm S(1) line to the in-band flux (Sect. 3.2).

Using a combination of the Hα and 24 μm luminosities, or the 7.7 μm PAH emission, Cluver et al. (2010) find an upper

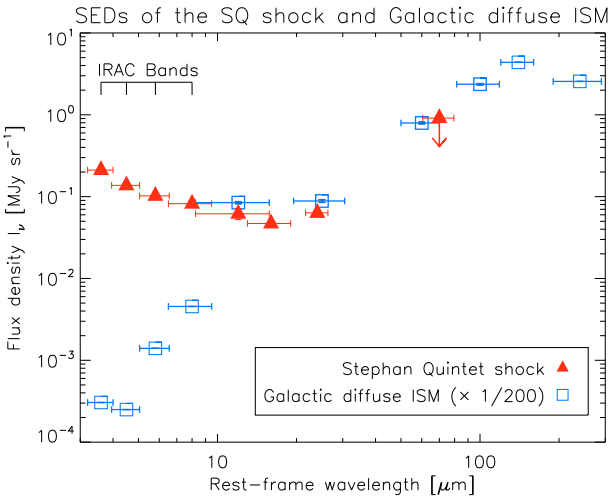

Fig. 2. The SED of the dust emission from the SQ shock seen by *Spitzer* (Table 1), compared to that of the Galactic diffuse emission observed with *Spitzer IRAC*, *IRAS*, and *DIRBE* towards the line-of-sight centered on the Galactic coordinates (28.6, +0.8). The contribution of the gas lines is subtracted. The Galactic SED is scaled down by a factor 200. Between 3−8 μm, the SQ flux is much brighter because of the stellar contribution. Horizontal bars indicate the filters bandwidths.

limit of $\lesssim$0.08 $M_\odot$ yr^{-1} to the star formation rate in the shock, as compared to ∼1.25 $M_\odot$ yr^{-1} in SQ-A. This suggests that the star formation is being depressed in the shock region.

4.2. Dust emission from the SQ shock, outside star-forming regions

The images and photometric measurements show that thermal dust emission is detected in the SQ shock structure, outside star-forming regions. The SED of the IR emission from the center of the shock is shown in Fig. 2. Among the SEDs listed in Table 1, the figure displays that of the last row (17″ beam, see Sect. 3).

For comparison with Galactic data, the figure includes a 12 μm flux computed by integrating the *IRS* spectrum over the IRAS 12 μm filter bandpass after subtraction of the gas lines. The 12/24 μm flux density ratio in the SQ shock is $\mathcal{F}_\nu^{(SQ)}(12\ \mu m)/\mathcal{F}_\nu^{(SQ)}(24\ \mu m) = 0.97 \pm 0.15$, which is remarkably close to the value for the Galactic diffuse ISM: $\mathcal{F}_\nu^{(MW)}(12\ \mu m)/\mathcal{F}_\nu^{(MW)}(25\ \mu m) = 0.95 \pm 0.07$. The Galactic SED is that measured towards the line-of-sight centered on the Galactic coordinates (28.6, +0.8), observed with the ISOCAM-CVF[4] and *Spitzer IRAC* (Flagey et al. 2006). Figure 2 also shows the *IRAS* 12, 25, 60, and 100 μm fluxes for the Galactic diffuse ISM emission measured on *IRIS* images (Miville-Deschênes & Lagache 2005). The *IRAS* SED is extended to 140 and 240 μm using *DIRBE* (Hauser et al. 1998) color ratios at the position of the line of sight. The total column density for this line of sight is estimated to be $N_H = 2\times10^{22}$ cm^{-2}, and the mean radiation field a few Habing units ($G_{UV} \sim 3$). In the figure, the Galactic SED is scaled down by a factor 200.

We propose that the faint dust emission we isolated at the center of the SQ shock is diffuse emission associated with the shocked molecular gas present in the ridge. A second possibility is that the dust is associated with the HI gas and a third one that it is produced by unresolved star-forming regions. We favor the first interpretation for three reasons.

- After inspecting the HI data of Williams et al. (2002), we see that the two outer contours in their Fig. 9, 0.6 and 1×10^{20} cm^{-2}, intersect our 17″ aperture used for dust photometry. Since the angular resolution of these HI observations is 20″, the HI emission is likely to be contaminated by beam smearing of the brighter emission to the north of our aperture. On the southern side of our aperture, in the ridge, HI is undetected and $N_{HI} < 5.8\times10^{19}$ cm^{-2}. This upper limit is smaller than the column density of warm H_2 (2×10^{20} cm^{-2}) derived from the *Spitzer* H_2 fluxes. Since the warm H_2 column density is a lower limit to the total H_2 column density, HI gas accounts for a minor fraction of the gas column density in the ridge. Therefore, the dust emission cannot be mostly associated with the HI gas in the shock region.
- *HST* observations show that there are very few star clusters in the center of the ridge. Most of them are associated with NGC 7319, the tidal debris of NGC 7318a/b, and the SQ-A intragroup starburst region (Gallagher et al. 2001). We find three candidates for star clusters (M_V = −12.14, −10.01, −9.65) within our 17″ (∼7.8 kpc) aperture in the center of the shock. These three clusters produce a V-band flux of 5.2×10^{-9} W m^{-2} sr^{-1}, which is 2 orders of magnitude lower than the V-band surface brightness that we derived from *HST* observations at the center of the ridge.
- The 12/24 μm flux ratio is remarkably similar to that of the Galactic diffuse ISM. The average column density of warm molecular gas in the SQ shock derived from H_2 observations is $N_H = 2\times10^{20}$ cm^{-2}, a factor of 100 smaller than that of the Galactic line of sight, in agreement with the scaling factor used to match the fluxes in Fig. 2.

4.3. Mid-IR spectroscopy: characterization of the dust emission from the SQ shock

4.3.1. *Spitzer IRS* spectrum in the center of the shock

The top panel of Fig. 3 presents a low-resolution *Spitzer IRS* spectrum extracted from a central position of the SQ ridge. This spectrum was obtained by Cluver et al. (2010), averaging all the spectra observed within a 274.2 arcsec^2 (∼18″×15″) rectangular aperture around the center of the ON position. These new data are of far higher sensitivity and have superior flux calibration than the first observations reported by Appleton et al. (2006). This spectrum confirms the first results discussed in Appleton et al. (2006). It exhibits bright S(0) to S(5) H_2 rotational lines, and forbidden atomic lines, including a remarkable 34.8 μm [Si II] feature. Here we focus on the dust emission.

The *IRS* spectrum shows that PAH and thermal dust emission is detected from the center of the SQ ridge, outside star-forming regions. A weak thermal continuum is also visible from 20 to 38 μm. The ratio of the fluxes of the 17 μm S(1) H_2 line to the 7.7 μm PAH feature is 1.2 ± 0.2 in the shock, which is about two orders of magnitude higher than the value observed in star-forming galaxies (Roussel et al. 2007).

4.3.2. PAH emission from the SQ shock

The 7.7, 11.3, and 17 μm aromatic infrared bands (AIBs), attributed to PAHs, are detected (although weak) in the new Cluver et al. (2010) observations at the center of the SQ shock. We used

[4] Camera equipped with a Circular Variable Filter (CVF) on-board the *Infrared Space Observatory* (ISO).

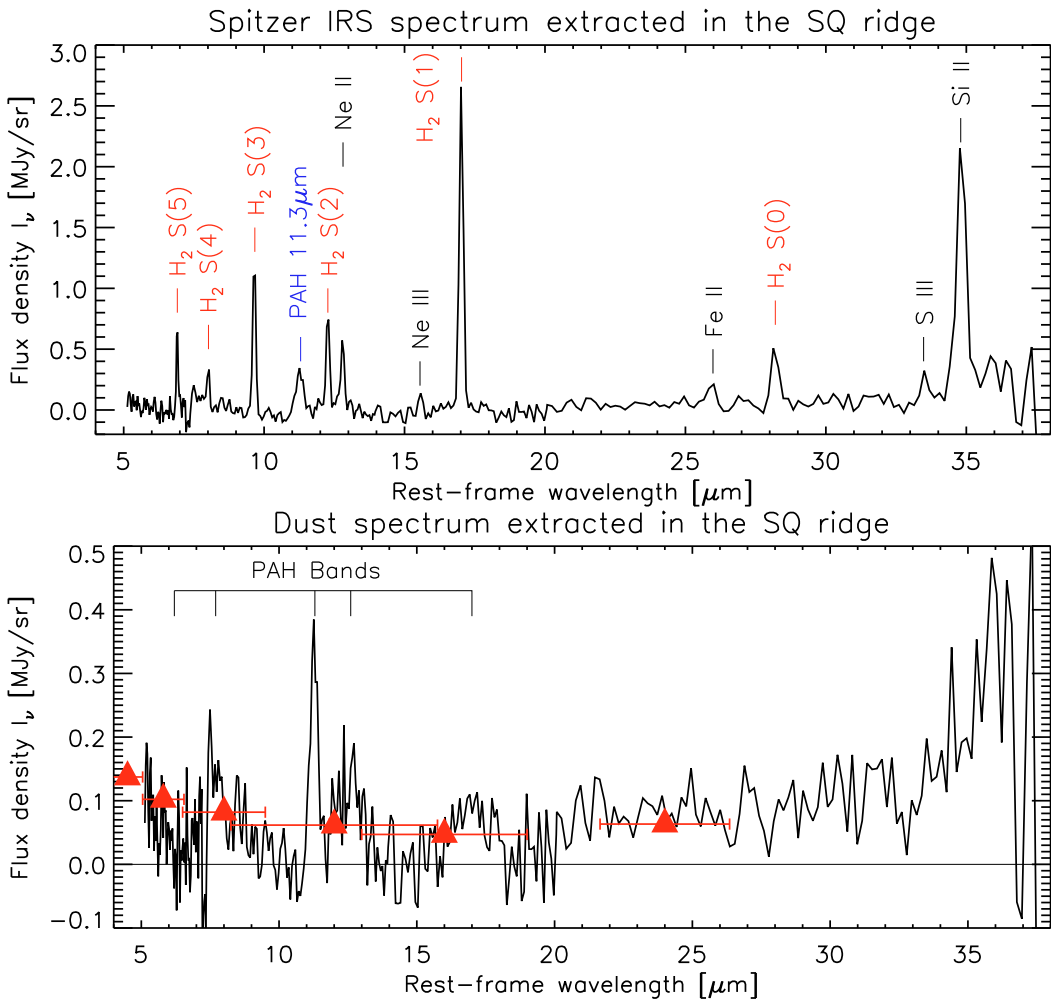

Fig. 3. *Spitzer IRS* mid-IR spectra extracted over a ∼18″ × 15″ area in the center of the SQ shock structure (RA 22:35:59.9, Dec +33:58:16.8). This aperture corresponds approximately to the "ON" beam shown in Fig. 1. *Top*: full spectrum. *Bottom*: gas lines are removed to highlight PAH dust features and thermal dust continuum. Photometric measurements (red triangles) performed on mid-IR images (same as in Table 1 and Fig. 2) are overplotted. Horizontal bars indicate the filters bandwidths.

the PAHFit IDL tool[5] (Smith et al. 2007) to decompose the full 5−38 μm *IRS* spectrum into contributions from PAH features, thermal dust continuum, starlight and gas lines. We do not include any extinction in the fit. The results of the fit to the full 5−38 μm spectrum is shown in Appendix A, Fig. A.1. This spectral decomposition allows us to remove the gas lines and extract a "pure" dust spectrum, shown on the bottom panel of Fig. 3. PAHFit is executed one more time on this spectrum, which allows us to measure accurately the fluxes of the AIBs. The line strengths of the PAH emission features and their ratios are gathered in Tables 4 and 5, respectively.

In Fig. 4, we compare the PAH spectrum from the SQ shock with the *ISOCAM-CVF* spectrum of the diffuse Galactic emission from Flagey et al. (2006), between 5 and 20 μm. The main differences between the two spectra are the following. First, the ratio of the flux in the band at 7.7 μm to the band at 11.3 μm (henceforth $R_{7.7/11.3}$) is a factor ∼2 lower for SQ ($R^{(SQ)}_{7.7/11.3}$ = 1.36 ± 0.07, see Table 5) than for the diffuse Galactic light ($R^{(MW)}_{7.7/11.3}$ = 2.93 ± 0.08). The $R_{7.7/11.3}$ value for the SQ shock is comparable to that measured for AGN of the *SINGS*[6] sample (Smith et al. 2007). Second, the 6.2 μm AIB is absent in the SQ spectrum. We note that the rise of the SQ spectrum at $\lambda < 6$ μm is due to the stellar component. The 17 μm complex is prominent but the 16.4 μm feature is not seen on top of it. This may not be significant because, to our knowledge, this feature is only prominent in the NGC 7023 Galactic PDR[7] (Sellgren et al. 2007). This feature is also observed in the star-forming galaxy NGC 7331 (Smith et al. 2004), but in a higher signal-to-noise-ratio spectrum than the one we have for SQ.

The enhancement of the 11.3 μm AIB relative to the 6.2, 7.7, and 8.6 μm features has been observed on galactic scales in elliptical galaxies (e.g., Kaneda et al. 2005), and in active galactic nuclei (e.g., Smith et al. 2007). This enhancement has also been discussed in the Galactic diffuse medium (e.g., Flagey et al. 2006) or at small scales, in PDR interfaces (e.g., Rapacioli et al. 2005; Compiègne et al. 2007).

The PAH emission spectrum depends on the size distribution, hydrogenation and ionization states. The $R_{7.7/11.3}$ PAH band

[5] Available at http://tir.astro.utoledo.edu/jdsmith/pahfit.php.

[6] Spitzer Infrared Nearby Galaxies Survey, http://sings.stsci.edu/.

[7] Photo-Dissociation Region.

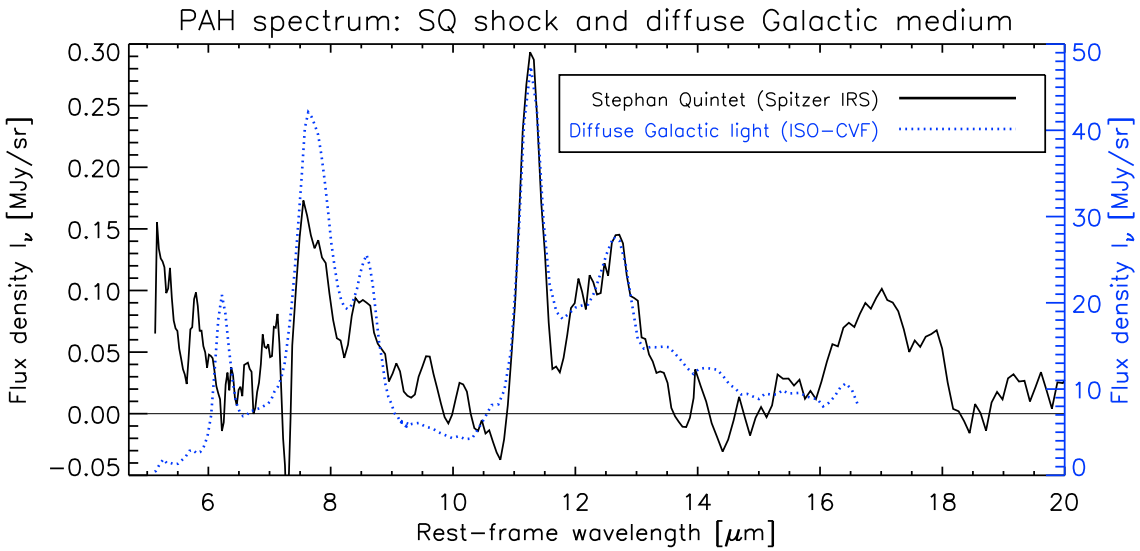

Fig. 4. *Spitzer IRS* PAH emission spectrum extracted at the center of the SQ ridge (black solid line), compared with the *ISOCAM-CVF* spectrum of the diffuse galactic medium (blue dashed line, with flux density labeled on the right). The *IRS* spectrum is smoothed to a resolution $\mathcal{R} = \lambda/\delta\lambda = 24 \rightarrow 51$, comparable with the *ISO-CVF* resolution ($\mathcal{R} = 35 \rightarrow 45$). Gas lines are removed in both spectra. Note that the flux scales are different for each spectrum (labels on the left for SQ, and on the right for the Galaxy).

Table 4. Fluxes of the PAH bands measured with the PAHFit IDL tool on the *Spitzer IRS* spectrum of the center of the SQ ridge and the *ISO-CVF* spectrum of the Galactic light.

	Integrated fluxes (see notes for units)				
PAH band	6.2 μm	7.7 μm^3	11.3 μm^3	12.6 μm^3	17 μm^3
SQ ridge *(IRS)*[1]	< 0.75	3.8 ± 0.1	2.8 ± 0.1	1.2 ± 0.2	0.93 ± 0.04
Galactic *(CVF)*[2]	5.19 ± 0.09	19.05 ± 0.03	6.49 ± 0.17	2.90 ± 0.05	No data

Notes. [(1)] Fluxes are in units of $\times 10^{-9}$ [W m^{-2} sr^{-1}].
[(2)] Fluxes are in units of $\times 10^{-7}$ [W m^{-2} sr^{-1}].
[(3)] In the case of PAH blended complexes, we sum the fluxes of the different Lorentzian components that contribute to the feature.

Table 5. Flux ratios of the PAH bands for the *Spitzer IRS* spectrum at the center of the SQ ridge, and the *ISO-CVF* spectrum of the diffuse Galactic light.

	Flux ratios			
	$R_{6.2/7.7}$	$R_{7.7/11.3}$	$R_{11.3/12.6}$	$R_{11.3/17}$
SQ ridge *(IRS)*	<0.2	1.36 ± 0.07	2.3 ± 0.2	3.01 ± 0.16
Galactic *(CVF)*	0.272 ± 0.005	2.93 ± 0.08	2.24 ± 0.07	No data

ratio depends mainly on the PAH ionization state. Theoretical (Langhoff 1996; Bakes et al. 2001a,b; Draine & Li 2001; Bauschlicher 2002) and experimental (e.g., Szczepanski & Vala 1993) studies show that neutral PAHs have lower $R_{7.7/11.3\ \mu m}$ than charged ones (both anions and cations). The charge state of PAHs is mainly determined by the ionization parameter $G_{UV}\sqrt{T}/n_e$, where G_{UV} is the integrated far ultraviolet (6−13.6 eV) radiation field expressed in units of the Habing radiation field, T is the electron temperature, and n_e is the electronic density. This parameter reflects the balance between photoionisation and recombination rates of electrons (Bakes & Tielens 1994; Weingartner & Draine 2001c). Flagey et al. (2006) quantified $R_{7.7/11.3\ \mu m}$ as a function of the ionization parameter $G_{UV}\sqrt{T}/n_e$ and the PAH mean size. We use their calculations to discuss the ionization state of the PAHs in the SQ shock. Our PAHFit decomposition yields $R_{7.7/11.3\ \mu m} = 1.36 \pm 0.07$, which translates into $G_{UV}\sqrt{T}/n_e \lesssim 30$ K$^{1/2}$ cm^3. Assuming a warm molecular gas temperature of $\sim$ 150 K and $G_{UV} = 1$, we find that $n_e \gtrsim 0.4$ cm^{-3}. This lower limit is one order of magnitude higher than the electronic densities inferred from observations and modeling of the ionization of cold neutral gas in the Solar neighbourhood (Weingartner & Draine 2001b). If this interpretation and diagnostic were to apply, a higher ionizing flux from cosmic-rays or X-rays would be required to maintain such a high electron density.

The $R_{6.2/7.7}$ PAH flux ratio depends on the size of the emitting PAHs (Draine & Li 2001). The non-detection of the 6.2 μm band sets a low upper limit of $R_{6.2/7.7} < 0.2$ to the PAH strength ratio, which is indicative of preferentially large PAHs. Although the method used by Draine & Li (2001) to measure the PAH line strengths differs from ours, we find that both $R_{7.7/11.3}$ and $R_{6.2/7.7}$ flux ratios in SQ can be explained by large (with a number of

carbon atoms $N_c \gtrsim 300$) and neutral PAHs in CNM conditions, excited with a $G_{UV} \simeq 1$ interstellar radiation field (see Fig. 17 of Draine & Li 2001).

5. Modeling dust emission

We present the physical framework and inputs of our modeling of the emission from dust associated with the molecular gas. Sections 5.1 and 5.2 present the codes and the radiation field that we use for our calculation of the dust emission.

5.1. The DUSTEM (Dust Emission) code

We use an updated version of the Désert et al. (1990) model, the *DUSTEM* code, to compute the dust emission. The modifications[8] implemented in the Desert et al. model are described in Compiègne et al. (2008). When the dust properties, the dust-to-gas mass ratio, and the incident radiation field are given, the code calculates the dust SED νS_ν in units of erg s^{-1} H^{-1}, for each dust grain species, as a function of the wavelength.

We use the diffuse Galactic ISM size distribution (a power-law $n(a) \propto a^{-3.5}$, Mathis et al. 1977), and dust-to-gas mass ratio inferred from the fitting of the SED and extinction curve of the diffuse ISM (Compiègne et al. 2008). The *DUSTEM* model includes a mixture of three populations of dust grains with increasing sizes:

- polycyclic aromatic hydrocarbons (PAHs) of radius a = 0.4−1.2 nm, responsible for the aromatic infrared bands (AIBs) and the FUV non-linear rise in the extinction curve.
- Very Small Grains (VSGs, a = 1−4 nm), which are carbonaceous (graphitic) nanoparticles producing the mid-IR continuum emission and the extinction bump at 2175 Å.
- Big Grains (BGs, $a = 4 - 110$ nm) of silicates with carbonaceous mantles or inclusions, which account for the far IR emission and the $1/\lambda$ rise in extinction at visible and near-IR wavelengths.

5.2. Radiation field

We model the radiation field used to compute the dust emission. Stellar radiation originates in the surrounding galaxies and/or stars in the ridge (Gallagher et al. 2001). The presence of ionizing radiation in the SQ ridge is also indicated by the lack of HI gas in the H_2-bright shock structure (Sulentic et al. 2001), and by emission from ionized gas lines. Optical line emission diagnostics suggest that shocks are responsible for hydrogen ionization in the ridge (Xu et al. 2003).

We therefore consider that the SED of the input radiation field consists of two components: a stellar component (Sect. 5.2.1), and photo-ionizing radiation from gas shocked at high-velocities (Sect. 5.2.2).

5.2.1. The interstellar radiation field (ISRF)

The photometry performed on NUV and FUV *GALEX* images shows that UV flux in the shock, outside star-forming regions, corresponds to an interstellar radiation field of intensity $G_{UV} = 1.4 \pm 0.2$ (see Table 2). What is the origin of this UV radiation in the shock? We estimate the UV emission in the ridge that comes from HII regions associated with star formation in the surrounding sources, i.e. NGC 7318a/b, the star-forming region SQ-A at the northern tip of the shock structure, and NGC 7319. The extinction-corrected FUV luminosities of these main sources surrounding the ridge are L_{FUV}(NGC 7318ab) = $8.1 \times 10^9\, L_\odot$, L_{FUV}(SQ-A) = $6.9{\times}10^9\, L_\odot$, and L_{FUV}(NGC 7319) = $6.9{\times}10^9\, L_\odot$ (Xu et al. 2005). Assuming that their distances to the center of the ridge are 10, 20 and 25 kpc, respectively, we find that the total UV flux in the ridge is $3.5{\times}10^{-3}$ erg s^{-1} cm^{-2}, i.e. $G_{UV} \simeq 1.5$ in Habing units. Most of the UV flux originates in NGC 7318a/b. Although this simple calculation does not take into account the extinction between the UV sources and the ridge, it shows that this estimate of the UV field is roughly consistent with our estimate from UV observations. The very small number (of the order of unity) of star clusters that lie within the center of the SQ shock (Gallagher et al. 2001) shows that their contribution to the UV field is small.

The SED of the stellar component of the radiation field is shown in Fig. 5 (green dashed line). We use the Mathis et al. (1983) ISRF, scaled by a factor of 1.4 to fit the FUV and NUV *GALEX* photometry. The *HST V*-band and *WIRC* near-IR photometric measurements (see Sect. 2.2.3 for observational details) are overlaid on Fig. 5 (see Table 3). The colors of the J, H, and K_s fluxes do not exactly match that of the (Mathis et al. 1983) radiation field, but we recall that these measurements are uncertain (because at these wavelengths, the radiation field is anisotropic, see Sect. 3.1.2). This effect does not significantly affect our dust modeling because the near-IR part of the radiation field has a small impact on the dust emission.

5.2.2. Photo-ionizing radiation field: shock and precursor components

In the shock sub-region, the [OI]6300 Å and [NII]6584 Å to Hα line ratios are ∼0.7 and ∼0.3, respectively, which is evidence of shock ionization (Xu et al. 2003). We therefore model the SED of the ionizing field using emission from a radiative shock. In the following, we constrain the shock parameters we use to model the emission from the ionized gas. The mid-IR *IRS* spectrum extracted from the core of the shock (Fig. 3) exhibits fine-structure line emission from [Ne II]λ 12.81 μm, [Ne III]λ 15.56 μm, [Fe II]λ 25.99 μm, [S III]λ 33.48 μm, and [Si II]λ 34.82 μm. The spatial distribution of this emission and mid-IR line diagnostics of the excitation mechanisms are discussed in Cluver et al. (2010). We summarize here the main results that are relevant to constraining the shock parameters.

The comparison between the high value of $\mathcal{F}_{[\mathrm{Ne\,II}]12.8}/\mathcal{F}_{[\mathrm{Ne\,III}]15.6} \sim 3.55$ and shock models (Hartigan et al. 1987; Allen et al. 2008) allows us to firmly constrain the range of shock velocities to be ∼80−200 km s^{-1} (Cluver et al. 2010). In the case of clumpy gas, if we were to consider the line emission from the shock only (discarding line emission from the pre-shock gas ionized by emission from the shocked gas), the upper limit to the shock velocities would be a little higher (300 instead of 200 km s^{-1}). In addition, the comparison of the [S III]λ 33.5 μm/[S III]λ 18.7 μm line ratios with these shock models constrains the pre-shock gas density to be $n_H \lesssim 10\,\mathrm{cm}^{-3}$. In the following, we therefore adopt a shock velocity of V_s = 100 km s^{-1} and a pre-shock density of n_H = 1 cm^{-3}. The photoionizing emission spectrum from shocked gas is taken

[8] In particular, the absorption cross-sections of the PAHs (with the addition of new aromatic infrared bands, AIBs) and the big grains (BGs), as well as the heat capacities (graphite, PAH C-H, silicate, and amorphous carbon) were updated.

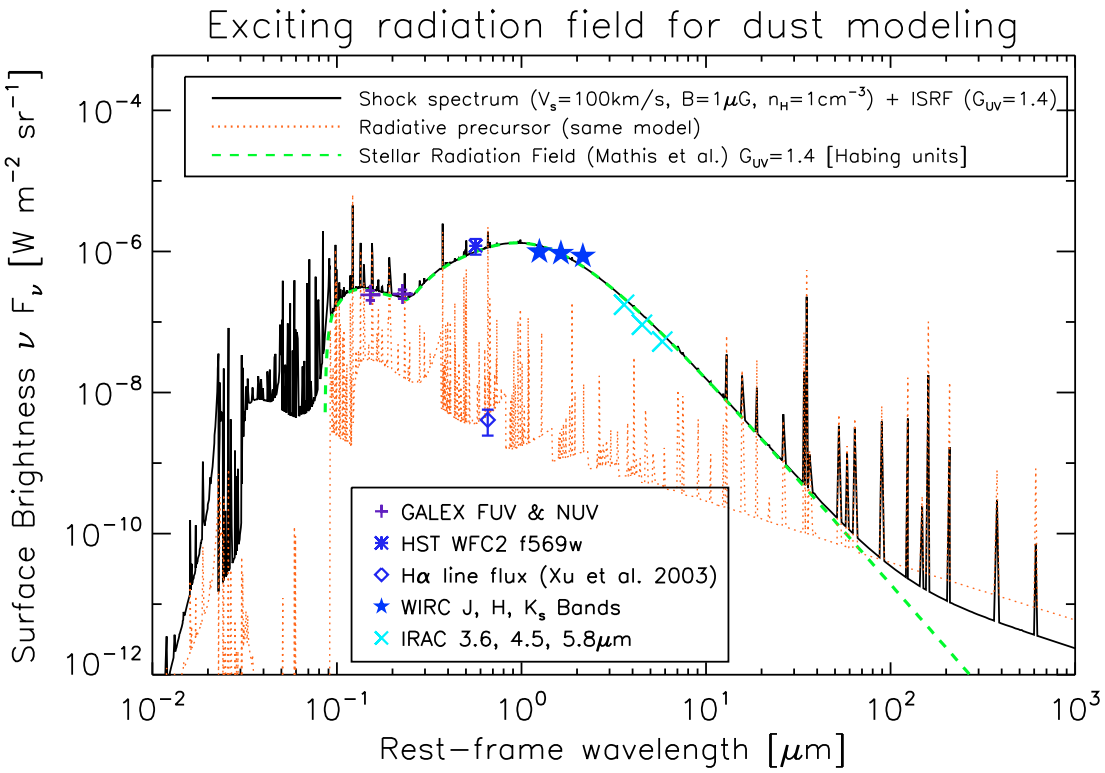

Fig. 5. The 2-component SED of the radiation field (stellar + shock) used as input for dust models to calculate the dust emission from molecular gas. The radiation field is the sum of an ISRF of intensity $G_{\rm UV} = 1.4$, scaled to match the observed UV flux in the shock, and the photoionizing spectrum of a $V_{\rm s} = 100$ km s^{-1} shock, scaled to match the Hα emission in the SQ ridge. The preshock gas density is $n_{\rm H} = 1$ cm^{-3} and the preshock magnetic field strength is $B_0 = 1$ μG.

from the library of the Mappings III shock code[9] (Allen et al. 2008). We normalize the shock spectrum to the observed Hα flux[10]. After this normalization, the SED of the ionizing shock emission is weakly sensitive to the two main shock parameters, the shock velocity and the gas density.

Figure 5 shows the SED of the radiation field that we use as input for the *DUSTEM* code to compute the outcoming dust emission from the molecular and ionized gas. The black solid line is the sum of the two contributions (stellar + shock) to the radiation field. The shock spectrum itself is mostly composed of thermal bremsstrahlung (free-free) continuum and resonance lines arising from many different elements and ionic stages. It also exhibits a prominent low-temperature bound-free continuum of hydrogen, produced in the cool, partially-ionized zone of the recombination region of the shock, and the strong hydrogen two-photon continuum produced mostly by the down-conversion of Lyα photons trapped in this same region of the shock structure. The bound-free continuum arising from the heavier elements is also present, though to a much weaker scale, with the helium continuum being the most obvious.

In the case of fast shocks ($V_{\rm s} > 100$ km s^{-1}), the shocked medium emits UV radiation that ionizes the pre-shock medium before it is shocked. A so-called *radiative precursor* propagates ahead of the shock, with an ionization front velocity that exceeds that of the shock. The contribution of the precursor itself is indicated in Fig. 5 by the red dotted line. The green dashed line shows the contribution of the $G_{\rm UV} = 1.4$ ISRF. The UV *GALEX*, Hα line, and near-IR *WIRC* fluxes in the center of the shock are indicated.

The contribution of the precursor to the total H II column density and radiative flux depends on the clumpiness of the preshock medium. This contribution is negligible if the molecular gas is clumpy, i.e. fragmented into dense ($n_{\rm H} > 10^3$ cm^{-3}) clouds that have a small volume filling factor, because most of the ionizing photons do not interact with neutral gas but with the volume-filling, hot plasma that is optically thin to ionizing radiation. However, diffuse H_2 gas is expected to have a much higher volume-filling factor. Our modeling of the dust emission from the ionized gas takes into account the precursor contribution, weighted by the volume-filling factor of the clumpy molecular gas.

6. On the structure of the molecular gas

The dust emission depends on the optical thickness of the molecular gas to UV radiation. Is the molecular gas diffuse or fragmented in optically thick clumps? In Sect. 6.1, we describe the assumptions we make about the structure of the molecular gas. We then present the results of our modeling of the dust emission in the SQ shock. We discuss the dust emission for the two physical structures of the H_2 gas presented in Sect. 6.1: diffuse (Sect. 6.2) and clumpy molecular gas (Sect. 6.3). Both models include the contribution of the ionized gas (H II) to the dust emission (this calculation is described in Sect. 6.4). This detailed modeling is fitted to mid-IR observations, and used to investigate the influence of the structure of the molecular gas on the FIR dust SED.

[9] http://cdsweb.u-strasbg.fr/~allen/mappings_page1.html

[10] $\mathcal{F}_{\rm H\alpha} = 4.1 \times 10^{-9}$ W m^{-2} sr^{-1} from Xu et al. (2003).

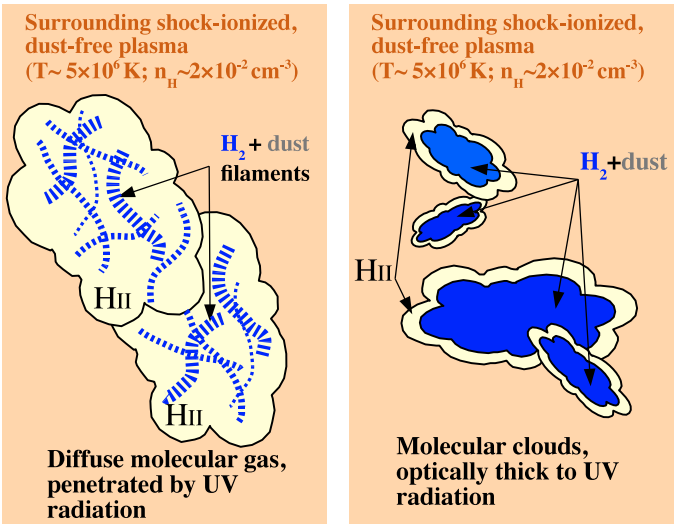

Fig. 6. Sketch of the two limiting physical states of the multiphase molecular gas we consider in the framework of our modeling of dust emission. (*Left*) Dust is associated with *diffuse* molecular gas that is broken into fragments, filaments, or sheets, penetrated by UV radiation. (*Right*) The dusty molecular gas is in clouds that are *optically thick* to UV light.

6.1. Two limiting cases for the structure of the molecular gas

The spectral energy distribution of the dust emission depends also on the structure of the molecular gas, and in particular on the optical depth of the clouds. The physical structure of the molecular gas in the SQ shock is an open question. In the following, we explore these two cases.

1. The molecular gas is *diffuse*, like the gas observed in the solar neighborhood by UV spectroscopy (e.g., Rachford et al. 2002) and across the Galaxy by observations of mid-IR H_2 line emission (Falgarone et al. 2005). In this case, we assume that the molecular gas is optically thin to UV radiation.
2. The molecular gas is within *clouds* that are *optically thick* to UV photons, as those observed in star-forming regions.

In a simplistic manner, Fig. 6 illustrates the two physical states (diffuse or clumpy) of the molecular gas we consider. In both cases, the molecular gas is embedded within HII gas and shock-heated, X-ray emiting plasma.

To compute the dust emission from optically thick (to UV photons) clouds (Fig. 6, right panel), we use the *Meudon PDR* (Photon Dominated Region) code (Le Petit et al. 2006) to compute the radiative transfer through the cloud. This 1-dimensional, steady-state model considers a stationary plane-parallel slab of gas and dust, illuminated by UV radiation. The radiation field output I_ν of the Meudon PDR code is used as input to the *DUSTEM* program to compute the spectral energy distribution (SED) of the dust as a function of the optical depth into the cloud. This 2-step process is iterated to take into account dust heating by the dust IR emission. Usually 4–5 iterations are needed before the radiation field converges.

6.2. Dust emission from diffuse molecular gas

The *DUSTEM* code is used to model the dust emission from diffuse molecular gas (Sect. 5.1), penetrated by UV photons. The cloud is illuminated by a composite field, made up of a stellar component (ISRF of intensity $G_{\rm UV}$ = 1.4 Habing units) and the ionizing radiation from the shocked gas (see Sect. 5.2 and Fig. 5). The dust properties are those of Sect. 5.1. The abundances and size distribution of the dust grains are Galactic. The dust emission from the ionized gas is included in the model SED. It is calculated separately with the *DUSTEM* code and added to the contribution of the cloud (see Sect. 6.4).

The top panel of Fig. 7 shows the 0.1–300 μm SED resulting from the model (black solid line), so that both the UV radiation field and IR dust emission can be seen. The dashed line (in the bottom right corner of the plot) shows the dust emission from the H II gas. The other three broken curves show the contributions of the different populations of dust grains, i.e., PAHs, VSGs, and BGs, respectively. The *GALEX*, *WIRC*, and *Spitzer* fluxes are indicated for comparison (see Sect. 3, Tables 1–3). The 7.7, 11.3, and 17 μm points are the peak values of the PAH bands detected in the *IRS* spectrum (Sect. 4.3). Other points come from imaging broadband photometry (GALEX, HST, IRAC, and MIPS) measurements performed in the center of the SQ ridge (over an aperture of 17″ in diameter, see Sect. 3).

The 11.3, 16 and 24 μm data points are used to fit the model SED. Since it may be a lower limit, the 70 μm point was not included in the fit. The gas column density is the only free parameter to fit the data. The model SED is obtained by multiplying the emissivity output of the *DUSTEM* code with the column density of warm molecular gas determined by fitting the SED to the mid-IR data. We find that the column density that most closely fits the data is $N_{\rm H} = 1.8 \pm 0.5 \times 10^{20}$ cm^{-2} for a Galactic dust-to-gas mass ratio. This column density obtained from the model is close to the column density derived from the H_2 line fluxes ($N_{\rm H} \simeq 2.2{\times}10^{20}$ cm^{-2}) within this aperture. This column density is obtained by fitting the rotational H_2 line fluxes with C-shocks models as described in Guillard et al. (2009). This suggests that the column density of cold ($T \lesssim 50$ K) molecular gas is much smaller than that of the warm H_2. However, this may not be the case because the dust-to-gas mass ratio is possibly lower than the Galactic value we assumed here, and the molecular gas may be in clumps optically thick to UV photons (see next section).

6.3. Dust emission from clumpy molecular gas

We model the dust emission associated with molecular gas fragmented into clumps that are optically thick to UV radiation. Here the *DUSTEM* and *Meudon PDR* codes (see Sect. 5.1) are combined to calculate the emission from a molecular cloud of total $A_V = 3$. The column density of the cloud is thus $N_{\rm H}^{\rm (c)} = 6.9 \times 10^{21}$ cm^{-2}. The choice of the A_V value is arbitrary. We check that the model SED in the mid-IR domain does not depend much on the total A_V because the mid-IR emission comes mainly from the surface of the cloud. The cloud is illuminated by a composite field (stellar + shock), consisting of the ISRF of intensity $G_{\rm UV}$ = 1.4 (Habing units) and the ionizing radiation from the shocked gas (see Sect. 5.2 and Fig. 5).

Figure 7 shows the sum of the outcoming radiation (cloud + ionized gas) emission spectrum and the incoming radiation, from the UV to the FIR (0.1–300 μm). The dashed line shows the emission from the ionized gas. The UV and IR photometric measurements are overlaid for comparison between data and models.

From UV to FIR wavelengths, the total SED (solid black line) consists of the ISRF, including the free-free, free-bound, and resonance line emission from the shocked gas, and the dust emission including the AIBs, the emission from the VSGs, and the grey body of the BGs at long wavelengths. The spectrum also exhibits some fine-structure IR lines, indicated in the spectrum,

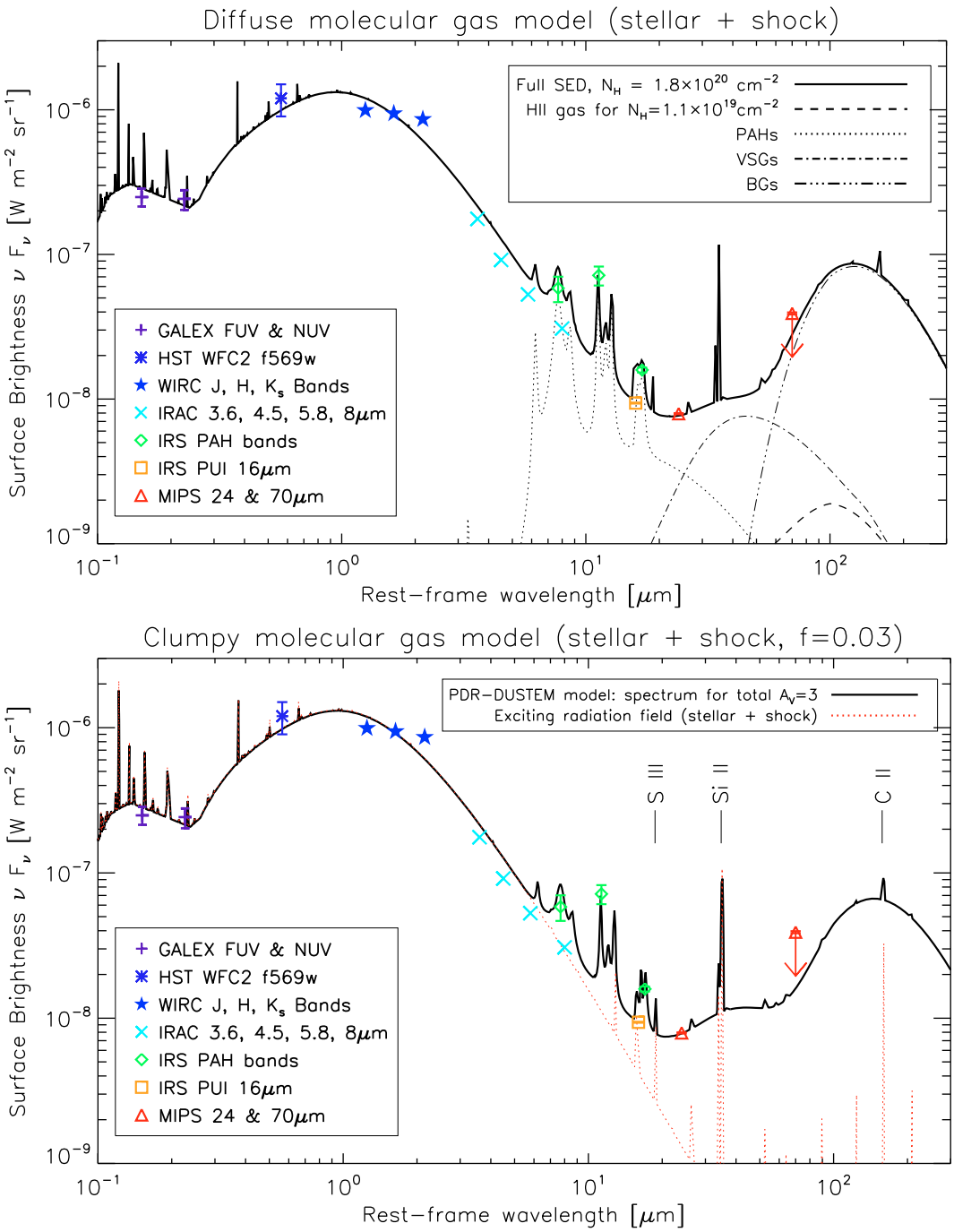

Fig. 7. SED of the dust emission associated with diffuse (*top*) or clumpy (*bottom*) molecular gas. The cloud is exposed to a radiation field consisting of a mixture (stellar + shock) of the Mathis et al. (1977) ISRF (scaled by a factor $G_{\rm UV} = 1.4$) and the ionizing emission spectrum of shock-heated gas for a shock velocity of 100 km s^{-1}. *(top)* The dashed line shows the contribution of the ionized gas (see text for details). The other broken lines show the different contributions of the three populations of grains (PAHs, VSGs, and BGs). We do not show them on the bottom figure for clarity. Assuming a Galactic dust-to-gas mass ratio, a column density of $N_{\rm H} = 1.8 \pm 0.5 \times 10^{20}$ cm^{-2} is needed to fit the *Spitzer* data. (*bottom*) The black solid line is the sum of the incoming and outgoing emission from a slab of gas of total $A_V = 3$, calculated with the *Meudon PDR* and *DUSTEM* codes. To fit the *Spitzer* data, the model IR emission is scaled by a factor $f = 0.03$, which represents the effective surface-filling factor of the molecular gas. The observed IRAC and MIPS fluxes correspond to the entries of Table 1. The green points are the IRS fluxes at the peak of the 7.7, 11.3, and 17 μm PAH bands.

e.g., 18.7 μm [S III], 34.8 μm [Si II], and 157.7 μm [C II]. To fit the data, the model IR emission from the cloud is scaled by a factor of $f = 0.03$, which represents an effective surface-filling factor for the molecular gas. The low value of f is consistent with the low value of the average optical extinction in the shock region. For clumps of $A_V = 3$, the average column density of the cloud phase is thus $\langle N_{\rm H} \rangle = f \times N_{\rm H}^{\rm (c)} \simeq 2.1 \times 10^{20}$ cm^{-2}. Our specific choice of $A_V = 3$ leads to a value of $\langle N_{\rm H} \rangle$ that is consistent with the column density of the warm H_2 gas seen by *Spitzer*. For larger values of A_V, the total column density of molecular gas will be larger than the column density of warm H_2 inferred from rotational lines.

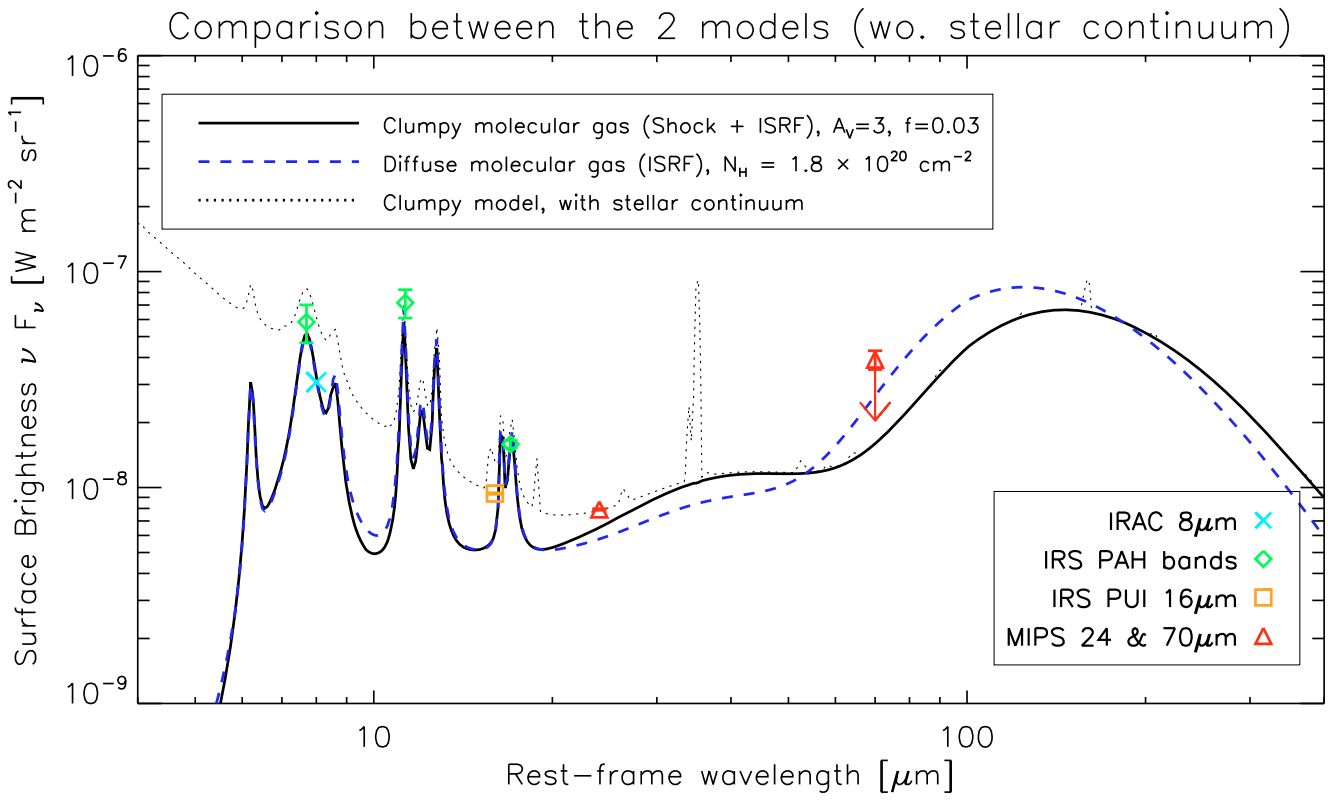

Fig. 8. Comparison between the two models presented in this paper: diffuse (dashed blue line, same model as Fig. 7) and clumpy (black line, same model as Fig. 7) molecular gas. The overlaid points indicate the *Spitzer* fluxes extracted within the shock region (see bottom right inset). The gas lines are removed from these spectra, as well as the IR component of the incident ISRF ($G_{\rm UV}$ = 1.4). For comparison, the clumpy model with stellar continuum is indicated by the thin black dotted (same model as Fig. 7).

6.4. Dust emission from shock- and precursor-ionized gas

We describe how we calculated the emission from dust associated with the ionized gas. This contribution was added to both models (diffuse and clumpy). We used the input radiation field of Fig. 5, including the ionizing part of the spectrum (λ < 912 Å), to compute the dust emissivity with the *DUSTEM* code. The column density of ionized gas was constrained by the integrated flux of the 12.8 μm [Ne II] fine-structure line, $\mathcal{F}_{\rm [Ne\,II]}$, measured on the *IRS* spectrum. The $\mathcal{F}_{\rm [Ne\,III]}/\mathcal{F}_{\rm [Ne\,II]}$ line flux ratio is low[11], which implies that Ne II is the main ionization state of Ne in the shock. Therefore, the column density of ionized gas can be expressed as

$$N_{\rm H}^{\rm (ion.gas)} = 2.3\times10^{19}\,\frac{\mathcal{F}_{\rm [Ne\,II]}\ [{\rm W\,m^{-2}\,sr^{-1}}]}{1.17\times10^{-9}}\,\frac{10\ {\rm cm^{-3}}}{n_{\rm e}}\ {\rm cm^{-2}}. \quad (1)$$

We used the relation between the [Ne II] line intensity and the emission measure given in Ho & Keto (2007) and we assumed that the electronic density of the 10^4 K gas is $n_{\rm e}$ = 10 cm^{-3}. This value is consistent with the SQ postshock pressure (~2 × 10^5 K cm^{-3}). The column density derived from Eq. (1) is comparable to the H II column density derived from the shock model ($N_{\rm H}$(H II)= 1.2 × 10^{19} cm^{-2} for a shock + precursor model at a shock velocity of 100 km s^{-1} and a preshock density $n_{\rm H}$ = 1 cm^{-3}).

The dust emission associated with this amount of ionized gas is the black dashed line in the top plot of Fig. 7. The column density of the ionized gas being one order of magnitude smaller than that of the warm H_2, the contribution of the ionized gas to the IR dust emission is negligible.

6.5. Comparison between models and degeneracies

Figure 8 shows the comparison between the result of the two models presented above. We focus on the dust emission, so the gas lines and the stellar continuum from the ISRF are removed from the spectra. The FIR SEDs are different between the two models. The FIR peak brightness of the SED of the diffuse molecular gas is brighter (by a factor of 1.7) and shifted towards shorter wavelengths than the clumpy model. This difference can be easily explained. When the molecular gas is clumpy, the dust grains see, on average, an attenuated radiation field, and are thus colder than in the diffuse model. For a given column density of matter, the FIR brightness is also fainter.

Current observations do not allow us to decide whether the gas is diffuse or fragmented into optically thick clumps. The spatial resolution of *Spitzer* at long wavelengths ($\lambda \gtrsim 70$ μm) is not high enough to obtain accurate photometric measurements. FIR observations with the *Herschel Space Telescope* will provide the sensitivity and angular resolution needed to test our models. However, it may not be so straightforward to conclude anything about the structure of the molecular gas because we assume a Galactic dust-to-gas mass ratio and size distribution. The IR SED also depends on the relative abundances of VSGs and BGs.

We defer the discussion about future observations needed to differentiate between the cloud structure and the dust size distribution to Sect. 8. We also note that we cannot estimate the total dust extinction from the models, given the lack of observational

[11] $\mathcal{F}_{\rm [Ne\,III]}/\mathcal{F}_{\rm [Ne\,II]}$ = 0.14 ± 0.04 in the center of the SQ ridge, see Table 3 in Cluver et al. (2010).

constraints in the FIR. The A_V value may be higher than the value derived from our modeling if the total H_2 column density including cold molecular gas is higher than that derived from the mid-IR H_2 rotational lines. If we assume that the molecular gas is diffuse and $N_H = 2 \times 10^{20}$ cm^{-2}, this corresponds to $A_V = 0.1$. This is smaller than the average value derived from optical observations ($A_V \sim 0.6$ in the main shock region for the diffuse emission).

7. Dust processing in the Stephan's Quintet shock?

The Stephan's Quintet galaxy-wide collision is an extreme environment where observations and modeling dust emission may provide insight into dust processing in shocks. The galaxy collision must have triggered shocks across the whole ISM. As discussed in Guillard et al. (2009), the shock velocity depends on the preshock gas density. Gas at preshock densities $n_H > 0.2$ cm^{-3} has been shocked at velocities small enough ($V_s < 200$ km s^{-1}) to cool, to keep most of its dust, and to become molecular within a few million years. To account for the H_2 emission, the molecular gas must be processed by low-velocity (5–20 km s^{-1}) MHD shocks, repeatedly. Therefore, the origin and dynamical state of the SQ molecular gas is very different from that of the Galactic ISM.

In the previous section, we assumed that the dust properties in the SQ ridge are identical to those of the Galaxy, which obviously is a simplifying assumption, that may be far from reality. In the shock region, various processes can affect dust grains (e.g., thermal sputtering of grains in the hot gas or destruction in shocks due to gas-grain and grain-grain interactions, see Jones 2004, and references therein) that can affect both the dust-to-gas mass ratio and the dust size distribution. To date, observational evidence of dust processing has come mainly from gas-phase depletions of metals (Sembach & Savage 1996). To our knowledge, there is no direct observational evidence of changes in the dust size distribution that can be unambiguously associated with shock-processing. Stephan's Quintet is an outstanding target to look for such evidence on galactic scales.

Dust destruction processes depend on the type of shocks. Guillard et al. (2009) show that within the timescale of the galaxy collision ($\sim 5 \times 10^6$ yr), the destruction of grains smaller than $\sim$0.1 μm is complete in the hot, teneous gas (corresponding to pre-shock densities $n_H \lesssim \times 10^{-2}$ cm^{-3}) that is shocked at high velocities ($V_s > 300$ km s^{-1}). For intermediate preshock densities ($n_H \sim 0.2$–0.01 cm^{-3}, $V_s = 100$–300 km s^{-1}), models predict significant dust destruction (10–50% in mass) and possibly the production of an excess of small grains by shattering (e.g., Jones & Tielens 1994). Within the dense ($n_H > 10^3$ cm^{-3}) molecular gas, low-velocity MHD[12] shocks (5–20 km s^1), may have little effect on dust (Guillet et al. 2007; Gusdorf et al. 2008).

The present SQ data provide some constraints on the dust size distribution. The detection of PAH emission from such a violent and extreme environment as the SQ shock may be seen as a surprise. PAHs are predicted to be completely destroyed for $V_s \gtrsim 125$ km s^{-1} ($n_H = 0.25$ cm^{-3}) and their structure would be deeply affected for $50 \lesssim V_s \lesssim 100$ km s^{-1} (Micelotta et al. 2010). The PAH detection therefore provides interesting constraints on the density structure of the preshock gas. Since it is unlikely that PAHs reform efficiently from carbon atoms in the postshock gas, we conclude that *(i)* they were protected from high-velocity shocks in high preshock density regions ($n_H \gtrsim 0.3$ cm^{-3}), or/and *(ii)* they are the products of the shattering of VSGs in the shock.

[12] Magneto-hydrodynamic

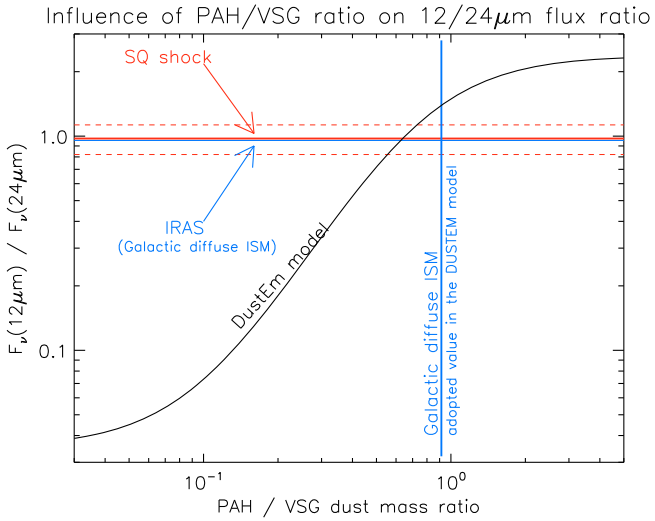

Fig. 9. Predicted 12/24 μm flux ratio from the *DUSTEM* model as a function of the PAH/VSG mass ratio. The horizontal red and blue lines shows the observed 12/24 μm flux ratios for the SQ shock, and the Galactic diffuse ISM (*IRAS* observations). The vertical blue line is the Galactic PAH/VSG ratio adopted in the model (0.915). This value is chosen to fit both the 12/24 μm ratio and the extinction curve.

We note that the 6.2 μm AIB is absent and that the 17 μm complex is prominent. This suggests that large PAHs, which emit more efficiently at longer wavelengths (e.g., Draine & Li 2007), are predominant in the shock. This may result from PAH processing in shocks, larger molecules being less fragile than smaller ones (Micelotta et al. 2010). This interpretation is supported by *Spitzer* observations by Tappe et al. (2006) that show a prominent 17 μm emission from the supernova remnant N132D in the Large Magellanic Cloud.

The 12/24 μm flux ratio is sensitive to the relative mass abundances of PAHs and VSGs. Figure 9 shows the predicted 12/24 μm flux ratio as a function of the PAH/VSG dust mass ratio. For each PAH/VSG ratio, the dust emission spectrum is calculated for an ISRF of $G_{UV} = 1.4$ with the *DUSTEM* code. We derive the 12 and 24 μm fluxes by integrating the model spectrum over the 12 μm *IRAS* and 24 μm *MIPS* filter bandpasses. The PAH/VSG mass ratio in the SQ shock is remarkably close to the value for the Galactic diffuse ISM. A deviation would be expected if the dust had been processed by high-speed (>100 km s^{-1}) shocks (Jones et al. 1996). As for PAHs, this suggests that the postshock dust was lying in gas dense enough to have been protected from destruction by fast shocks, and thus was protected from the effect of fast shocks, as proposed by Guillard et al. (2009). However, as discussed in Sect. 4.3.2, the PAH spectrum in the shock is significantly different from that observed in the diffuse Galactic ISM. The fact that the long wavelength bands (11.3 and 17 μm) are brighter than the 6.2 and 7.7 μm features imply that a higher fraction of the PAH emission is emitted within the 12 μm IRAS band. If this were true, this correction would imply a lower PAH/VSGs abundance than in the Galactic diffuse ISM.

Far-IR SED imaging of the dust, possible with the PACS[13] and SPIRE[14] instruments onboard *Herschel*, combined with modeling of the full IR spectral energy distribution, would provide diagnostics for measuring the relative abundances of the different grain populations.

[13] Photodetector Array Camera and Spectrometer.
[14] Spectral and Photometric Imaging Receiver.

In our modeling (Sect. 6), we did not consider any thermal emission from collisionally heated dust in the hot plasma. This emission may arise after a fast shock wave traveled through tenuous, dusty gas, but it will last a very short period of time ($\sim 10^6$ yr), producing a "flash" of FIR emission, because the dust cooling efficiency drops as the grain sputtering occurs in the hot ($>10^6$ K) gas (Smith et al. 1996; Guillard et al. 2009). However, there are two reasons why this may not be a valid assumption. First, if there is significant dust mass in grains larger than about 0.3 μm, this dust may survive for $\gtrsim 5 \times 10^6$ yr. These grains may contribute to the FIR emission, as proposed by Xu et al. (2003) and further investigated by Natale et al. (in prep.). Second, we cannot exclude that some dust may be injected into the hot phase by the ablation of clouds (turbulent mixing), due to their dynamical interaction with the background plasma (Guillard et al. 2009). A continuous supply of dust from the warm to hot phase could balance destruction by sputtering. This possibility needs to be quantified, but was beyond the scope of this paper.

8. Summary and concluding remarks

In this paper, we have presented new *Spitzer* imaging and spectroscopic observations that reveal PAH and VSG emission from the galaxy-scale shock in Stephan's Quintet (SQ). We now provide our main observational results:

- Faint dust emission was detected at the center of the H_2-bright SQ shock structure, outside star-forming regions lying in the SQ halo. The 12/24 μm flux density ratio in the SQ ridge is remarkably similar to that of the diffuse Galactic ISM. This suggests that the PAH to VSG abundance ratio is similar to that of the diffuse ISM of the Galaxy.
- The global mid-IR SED is consistent with the expected dust emission from the amount of warm H_2 detected by *Spitzer* ($N_{\rm H} \simeq 2 \times 10^{20}$ cm^{-2}) for a UV radiation field intensity of $G_{\rm UV} \sim 1$ [Habing unit], which is consistent with UV observations of the shock.
- The PAH emission spectrum in the SQ shock differs significantly from that of the diffuse Galactic ISM. The 7.7, 11.3, and 17 μm aromatic bands are detected, but the 6.2 μm band is absent. The 17 μm complex is prominent, but the 16.4 μm is not detected. Interestingly, the 7.7/11.3 μm flux ratio in the SQ shock is a factor ~2 lower than that of the diffuse Galactic PAHs. These characteristics may be indicative of an enhanced fraction of neutral and large PAHs.

Spitzer imaging and spectroscopy reveal powerful H_2 emission in the Stephan's Quintet X-ray giant shock that extends over the full area ($\approx 35 \times 15$ kpc^2) of the ridge (Cluver et al. 2010). We expect some dust emission to originate in molecular gas because H_2 forms on dust grains. In this paper we have tested this interpretation by modeling the IR emission from dust associated with the H_2 gas present in the SQ shock structure, and by comparing the model calculations with *Spitzer* observations.

- We have modeled the emission from dust associated with diffuse or clumpy molecular gas, embedded within HII gas and X-ray emitting plasma. The model SED is consistent with mid-IR *Spitzer* observations for both cases, for a Galactic dust-to-gas mass ratio and a Galactic dust size distribution. For diffuse gas, the best-fit column density is $N_{\rm H} = 1.8 \pm 0.5 \times 10^{20}$ cm^{-2}, which is close to the value derived from warm H_2 observations. For clumpy molecular clouds that are optically thick to UV radiation, we found that the H_2 surface filling factor is $f \sim 0.03$. So far, the present data and the degeneracy between the dust size distribution and the cloud structure do not allow us to decide whether the molecular gas is diffuse or fragmented into clouds that are optically thick to UV photons.
- The presence of dust in the SQ shock shows that dust is able to survive in such a violent environment. We propose that at the time of the high-speed galaxy encounter, the dust that survived destruction was in pre-shock gas of density higher than a few 0.1 cm^{-3}, which had not been shocked at velocities larger than ~200 km s^{-1} (see Guillard et al. 2009). Current data do not allow us to identify a plausible impact of the shock on the dust size distribution, but the peculiar properties of the PAH emission in the SQ ridge (summarized above) may be the result of PAH processing in shocks.

Future far-IR observations are needed to constrain both the structure of the H_2 gas and the dust properties in the SQ shock. The PACS and SPIRE instruments on *Herschel* would provide data from which we could reconstruct the SED of the far-IR dust emission resolved on scales of 5−10 arcsecs, crucial for helping us to determine how clumpy the dust distribution is in the shock structure. The flux in the FIR is different for the two models (diffuse or clumpy, see Fig. 8). The spatial resolution of the PACS [60−210 μm] instrument on-board the *Herschel Space Observatory* at 70 μm is comparable to that of *Spitzer* at 24 μm. It will thus be possible to extract the FIR emission from the shock with much more accuracy than possible with *Spitzer*. This is needed to help break some degeneracies in the model and more tightly constrain the key-parameters (e.g., dust size distribution).

The Stephan's Quintet galaxy-collision is a unique environment for studying dust survival in shocks, on galactic scales. The presence of dust in the SQ shock highlights the need to revisit the standard calculations of dust survival timescales in the ISM, by taking into account its multiphase structure.

Acknowledgements. This work is partly based on observations made with the Spitzer Space Telescope, which is operated by the Jet Propulsion Laboratory, California Institute of Technology under a contract with NASA.
GALEX (Galaxy Evolution Explorer) is a NASA small explorer launched in 2003 April. We gratefully acknowledge NASA's support for construction, operation, and science analysis for the GALEX mission, developed in cooperation with the Centre National d'Etudes Spatiales (CNES) of France and the Korean Ministry of Science and Technology.
This research has made use of the NASA/IPAC Extragalactic Database (NED) which is operated by the Jet Propulsion Laboratory, California Institute of Technology, under contract with the National Aeronautics and Space Administration.
P.G. would like to thank M. Gonzalez Garcia and J. Le Bourlot for help about the PDR code, and V. Guillet for helpful discussions about dust processing in shocks. We wish to aknowledge R. Tuffs, C. Popescu, G. Natale and E. Dwek for fruitful discussions we had about dust emission in SQ. The authors are indebted to V. Charmandaris for having provided his deep near-IR images of Stephan's Quintet taken with the *WIRC* instrument on the Palomar 200-inches telescope. We are grateful to M.G. Allen for making publicly available the *Mappings III* shock library. We also thanks the anonymous referee for useful comments that helped us improve the clarity of the manuscript and for having suggested the use of optical data.

Appendix A: Fitting PAH features

The results of the PAHFit decompositions of the *Spitzer IRS* spectrum of the center of SQ ridge and, for comparison, of the *ISO-CVF* spectrum of the diffuse Galactic medium, are presented in Figs. A.1, A.2, and A.3. No extinction parameter was introduced into the fit.

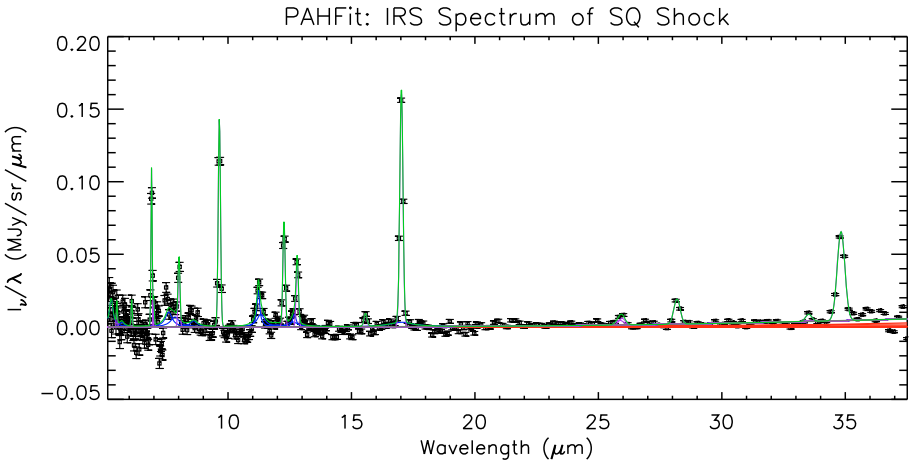

Fig. A.1. Result of a PAHFit model fit on the 5−38 μm *Spitzer IRS* spectrum extracted over a ∼18″ × 15″ area centered on the position of the center of the ridge (ON beam in Fig. 1). The green line shows the complete model. The fitted gas lines are in magenta. The Gaussian profiles of the gas lines are used to remove their contributions and extract a "pure dust spectrum" (see Fig. A.2).

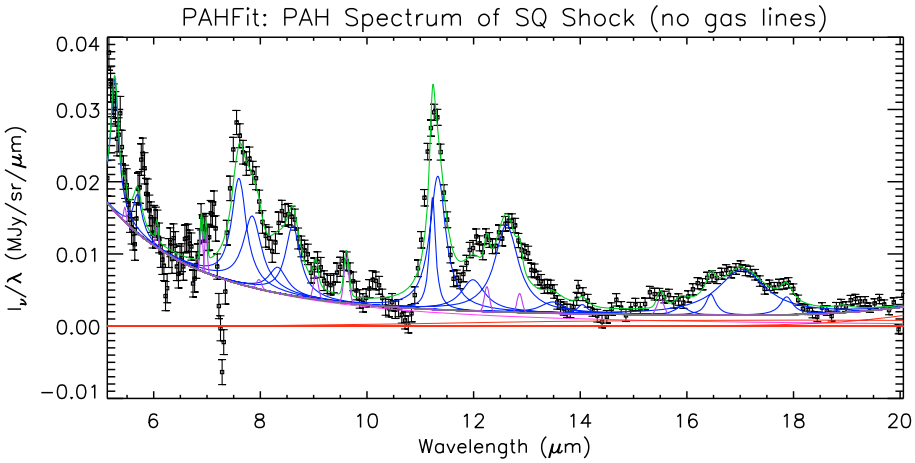

Fig. A.2. PAHFit decomposition of the *Spitzer IRS* dust spectrum (smoothed over 5 resolution elements, and from which gas lines have been removed) extracted from the center of the SQ ridge. Blue solid lines shows the Lorentzian components of the PAH decomposition, and the thick gray line is the total (dust + starlight) continuum. The result of the fit is the green solid line.

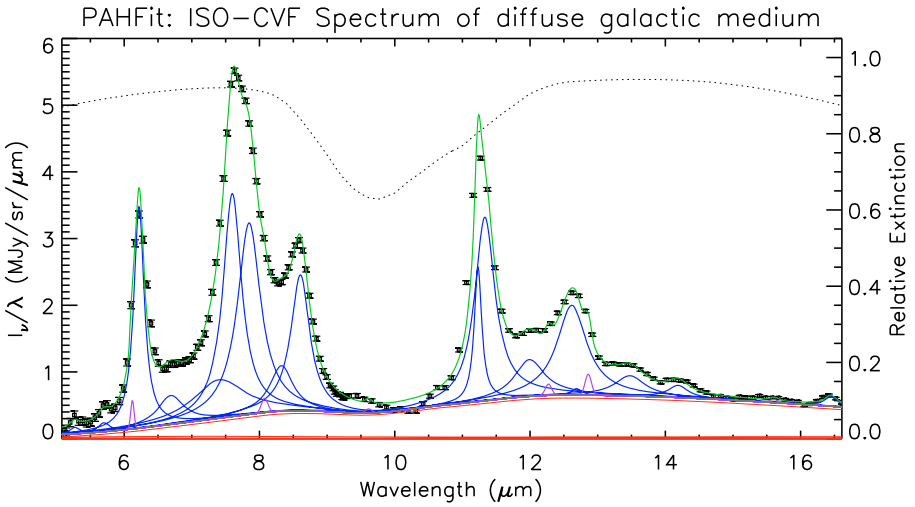

Fig. A.3. PAHFit decomposition of the *ISO-CVF* spectrum of the diffuse Galactic light (Flagey et al. 2006), centered on the Galactic coordinates (26.8, +0.8). The gas lines have been removed from the spectrum. The Lorentzian components of the decomposition of the PAH features are shown in blue. All components are diminished by the extinction, indicated by the dotted black line, with axis at right. The solid green line is the full fitted model, plotted on the observed flux intensities and uncertainties.

References

Allen, M. G., Groves, B. A., Dopita, M. A., Sutherland, R. S., & Kewley, L. J. 2008, ApJS, 178, 20
Allen, R. J., & Hartsuiker, J. W. 1972, Nature, 239, 324
Allen, R. J., & Sullivan, III, W. T. 1980, A&A, 84, 181
Appleton, P. N., Xu, K. C., Reach, W., et al. 2006, ApJ, 639, L51
Bakes, E. L. O., & Tielens, A. G. G. M. 1994, ApJ, 427, 822
Bakes, E. L. O., Tielens, A. G. G. M., & Bauschlicher, C. W. 2001a, ApJ, 556, 501
Bakes, E. L. O., Tielens, A. G. G. M., jr, Bauschlicher, C. W., Hudgins, D. M., & Allamandola, L. J. 2001b, ApJ, 560, 261
Bauschlicher, Jr., C. W. 2002, ApJ, 564, 782
Cazaux, S., & Tielens, A. G. G. M. 2004, ApJ, 604, 222
Cluver, M. E., Appleton, P. N., Boulanger, F., et al. 2010, ApJ, 710, 248
Cohen, M., Wheaton, W. A., & Megeath, S. T. 2003, AJ, 126, 1090
Compiègne, M., Abergel, A., Verstraete, L., et al. 2007, A&A, 471, 205
Compiègne, M., Abergel, A., Verstraete, L., & Habart, E. 2008, A&A, 491, 797
Désert, F.-X., Boulanger, F., & Puget, J. L. 1990, A&A, 237, 215
Draine, B. T., & Li, A. 2001, ApJ, 551, 807
Draine, B. T., & Li, A. 2007, ApJ, 657, 810
Falgarone, E., Verstraete, L., Pineau Des Forêts, G., & Hily-Blant, P. 2005, A&A, 433, 997
Fazio, G. G., Hora, J. L., Allen, L. E., et al. 2004, ApJS, 154, 10
Flagey, N., Boulanger, F., Verstraete, L., et al. 2006, A&A, 453, 969
Gallagher, S. C., Charlton, J. C., Hunsberger, S. D., Zaritsky, D., & Whitmore, B. C. 2001, AJ, 122, 163
Gao, Y., & Xu, C. 2000, ApJ, 542, L83
Guillard, P., Boulanger, F., Pineau Des Forêts, G., & Appleton, P. N. 2009, A&A, 502, 515
Guillet, V., Pineau Des Forêts, G., & Jones, A. P. 2007, A&A, 476, 263
Gusdorf, A., Cabrit, S., Flower, D. R., & Pineau Des Forêts, G. 2008, A&A, 482, 809
Habing, H. J. 1968, Bull. Astron. Inst. Netherlands, 19, 421
Hartigan, P., Raymond, J., & Hartmann, L. 1987, ApJ, 316, 323
Hauser, M. G., Arendt, R. G., Kelsall, T., et al. 1998, ApJ, 508, 25
Ho, L. C., & Keto, E. 2007, ApJ, 658, 314
Houck, J. R., Roellig, T. L., van Cleve, J., et al. 2004, ApJS, 154, 18
Jones, A., & Tielens, A. 1994, The Cold Universe, XIIIth Moriond Astrophysics Meeting, ed. T. Montmerle, C. Lada, I. Mirabel, & J. Thanh Van (Gif-sur Yvette: Éditions Frontières)
Jones, A. P. 2004, in Astrophysics of Dust, ed. A. N. Witt, G. C. Clayton, & B. T. Draine, ASP Conf. Ser., 309, 347
Jones, A. P., Tielens, A. G. G. M., & Hollenbach, D. J. 1996, ApJ, 469, 740
Kaneda, H., Onaka, T., & Sakon, I. 2005, ApJ, 632, L83
Langhoff, S. 1996, J. Phys. Chem., 100, 2819
Le Petit, F., Nehmé, C., Le Bourlot, J., & Roueff, E. 2006, ApJS, 164, 506
Lisenfeld, U., Braine, J., Duc, P.-A., et al. 2002, A&A, 394, 823
Martin, D. C., Fanson, J., Schiminovich, D., et al. 2005, ApJ, 619, L1
Mathis, J. S., Rumpl, W., & Nordsieck, K. H. 1977, ApJ, 217, 425
Mathis, J. S., Mezger, P. G., & Panagia, N. 1983, A&A, 128, 212
Micelotta, E. R., Jones, A. P., & Tielens, A. G. G. M. 2010, A&A, 510, A36+
Miville-Deschênes, M.-A. & Lagache, G. 2005, ApJS, 157, 302
Moles, M., Sulentic, J. W., & Marquez, I. 1997, ApJ, 485, L69+
Morrissey, P., Conrow, T., Barlow, T. A., et al. 2007, ApJS, 173, 682
O'Sullivan, E., Giacintucci, S., Vrtilek, J. M., Raychaudhury, S., & David, L. P. 2009, ApJ, 701, 1560
Pietsch, W., Trinchieri, G., Arp, H., & Sulentic, J. W. 1997, A&A, 322, 89
Popescu, C. C., Tuffs, R. J., Fischera, J., & Völk, H. 2000, A&A, 354, 480
Rachford, B. L., Snow, T. P., Tumlinson, J., et al. 2002, ApJ, 577, 221
Rapacioli, M., Joblin, C., & Boissel, P. 2005, A&A, 429, 193
Rieke, G. H., Young, E. T., Engelbracht, C. W., et al. 2004, ApJS, 154, 25
Roussel, H., Helou, G., Hollenbach, D. J., et al. 2007, ApJ, 669, 959
Sellgren, K., Uchida, K. I., & Werner, M. W. 2007, ApJ, 659, 1338
Sembach, K. R., & Savage, B. D. 1996, ApJ, 457, 211
Smith, B. J., & Struck, C. 2001, AJ, 121, 710
Smith, J. D. T., Dale, D. A., Armus, L., et al. 2004, ApJS, 154, 199
Smith, J. D. T., Draine, B. T., Dale, D. A., et al. 2007, ApJ, 656, 770
Smith, R. K., Krzewina, L. G., Cox, D. P., Edgar, R. J., & Miller, W. W. I. 1996, ApJ, 473, 864
Sulentic, J. W., Rosado, M., Dultzin-Hacyan, D., et al. 2001, AJ, 122, 2993
Szczepanski, J., & Vala, M. 1993, ApJ, 414, 646
Tappe, A., Rho, J., & Reach, W. T. 2006, ApJ, 653, 267
Trinchieri, G., Sulentic, J., Breitschwerdt, D., & Pietsch, W. 2003, A&A, 401, 173
Trinchieri, G., Sulentic, J., Pietsch, W., & Breitschwerdt, D. 2005, A&A, 444, 697
Weingartner, J. C., & Draine, B. T. 2001a, ApJ, 548, 296
Weingartner, J. C., & Draine, B. T. 2001b, ApJ, 563, 842
Weingartner, J. C., & Draine, B. T. 2001c, ApJS, 134, 263
Williams, B. A., Yun, M. S., & Verdes-Montenegro, L. 2002, AJ, 123, 2417
Xu, C., Sulentic, J. W., & Tuffs, R. 1999, ApJ, 512, 178
Xu, C. K., Lu, N., Condon, J. J., Dopita, M., & Tuffs, R. J. 2003, ApJ, 595, 665
Xu, C. K., Iglesias-Páramo, J., Burgarella, D., et al. 2005, ApJ, 619, L95
Xu, C. K., Appleton, P. N., Dopita, M., et al. 2008, in Infrared Diagnostics of Galaxy Evolution, ed. R.-R. Chary, H. I. Teplitz, & K. Sheth, ASP Conf. Ser., 381, 88